Gaseous Argon Optical Time Projection Chamber Technology Demonstration for the Deep Underground Neutrino Experiment (DUNE) Near Detector

Raheema Hafeji

Master of Science by Research

University of York
School of Physics, Engineering and Technology

June 2025

Abstract

The Deep Underground Neutrino Experiment will study neutrinos produced from a high-intensity beam, that will travel a distance of over 1,300 km. One component of the near detector site that will be located less than 600 m from the source of the beam is ND-GAr, a high-pressure gaseous argon-based Time Projection Chamber. GAT0 is the name of a prototype of ND-GAr being developed to demonstrate event time-tagging with primary scintillation light that is produced after particle interactions, a n d imaging of ionisation tracks. By doping argon with 1% of CF_4, scintillation light is wavelength-shifted from the VUV to the visible region centred at λ= 630 nm, a region that is easier to detect with readily available photosensors,

Imaging of alpha particle ionisation tracks from secondary scintillation light in GAT0 is demonstrated by instrumenting two layers of micropatterned charge amplification structures - thick Gaseous Electron Multipliers - operated in 1 bar of Ar:CF_4 at a concentration of 99:1.

Primary scintillation light will be used to record the absolute time of interactions and will be detected with a plane of SiPM photosensors. The time resolution of the photosensor limits how precisely this information can be retrieved. A front-end readout electronics board that combined the readout of 16 channels of the Hamamatsu S14161-6050HS-04 SiPM tile to pave the way for large-area coverage was developed for GAT0. Experimental results show a signal-to-noise ratio of 7 and a dark count rate of $\sim$500 at -35 °C.

A layer of reflective PTFE material is placed surrounding the inner surface of GAT0, to increase the light collection efficiency. Photon propagation simulations were carried out in Geant4 with a range of PTFE reflectance values, and two scenarios of SiPM area-coverage are presented.

Contents

List of Figures

Author's declaration

I declare that this thesis is a presentation of original work and I am the sole author. This work has not previously been presented for a degree or other qualification at this University or elsewhere. All sources are acknowledged as references.

The research project was carried out at Instituto de F´ısica Corpuscular (Val`encia, Spain) and Instituto Galego de F´ısica de Altas Enerx´ıas (Santiago de Compostela, Spain). The local supervisors were Dr. Justo Mart´ın-Albo and Prof. Diego González D´ıaz.

The design of the SiPM readout electronics board described in this work was produced by Carlos Gaspar Ben´ıtez Montiel, an Electronics Engineer in the Neutrino Group of Instituto de F´ısica Corpuscular.

Chapter 1

Introduction

1.1 The Deep Underground Neutrino Experiment

The Deep Underground Neutrino Experiment (DUNE) is a next generation experiment and international collaboration, being built to probe neutrino interactions to unravel some of the most intriguing mysteries in particle physics and astrophysics. As neutrinos travel, they oscillate between their 3 flavours; electron ($\nu_e/\bar{\nu}_e$), muon ($\nu_\mu/\bar{\nu}_\mu$) and tau ($\nu_\tau/\bar{\nu}_\tau$). In order for them to oscillate, neutrinos must possess a small mass, which goes beyond the Standard Model for physics.

DUNE seeks to understand the dominance of matter over antimatter in the universe, by observing the differences in behaviour between neutrino and antineutrino oscillations. The experiment will send a high-intensity neutrino beam provided by the Long-Baseline Neutrino Facility (LBNF) to an underground detector complex in Fermilab - the near detector - that will be located close to the beam target from where the neutrinos originate. The neutrinos will then travel to more than 1,300 km away, to a far detector that is approximately 1.5 km underground at the Sanford Underground Research Facility (figure 1.1 [1]). The far detector will measure the beam originating at Fermilab, and also atmospheric and astrophysical neutrinos.

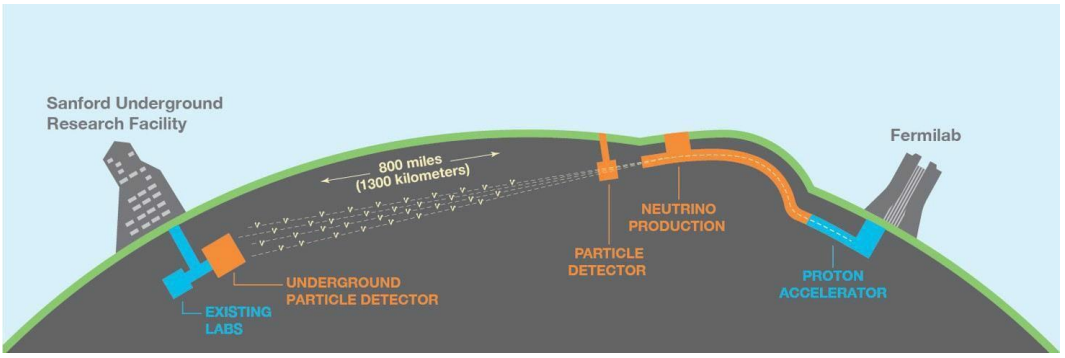

Figure 1.1: The DUNE experimental sites at Fermilab and the Sanford Underground Research Facility [1].

A key aim of the DUNE experiment is to measure the rate of neutrino interactions, from which the oscillation probabilities for muon (anti)neutrinos to oscillate to electron (anti)neutrinos or remain the same flavour can be extracted. By determining the probability as a function of neutrino energies, precision measurements of the oscillation parameters can be carried out. The near detector will measure the un-oscillated neutrino interaction rate, and the far detector will measure the oscillated neutrino interaction rate. By comparison of spectra taken at both the near and far detectors, the oscillation probabilities will be determined. DUNE will also be sensitive to rare proton decay signals, that have been theorised but not detected so far, which will make progress towards the unified theory of matter and energy. Furthermore, DUNE will detect supernova neutrino bursts (SNBs) to study neutron stars and black holes.

1.2 ND-GAr

1.2.1 Components and design

The near detector [2] will consist of three primary components: a magnetised high-pressure gaseous argon-based Time Projection Chamber (ND-GAr), a liquid argon Time Projection Chamber (ND-LAr), and a magnetised beam monitor that is named System for on-Axis Neutrino Detection (SAND). A schematic of the near detector is shown in figure 1.2.

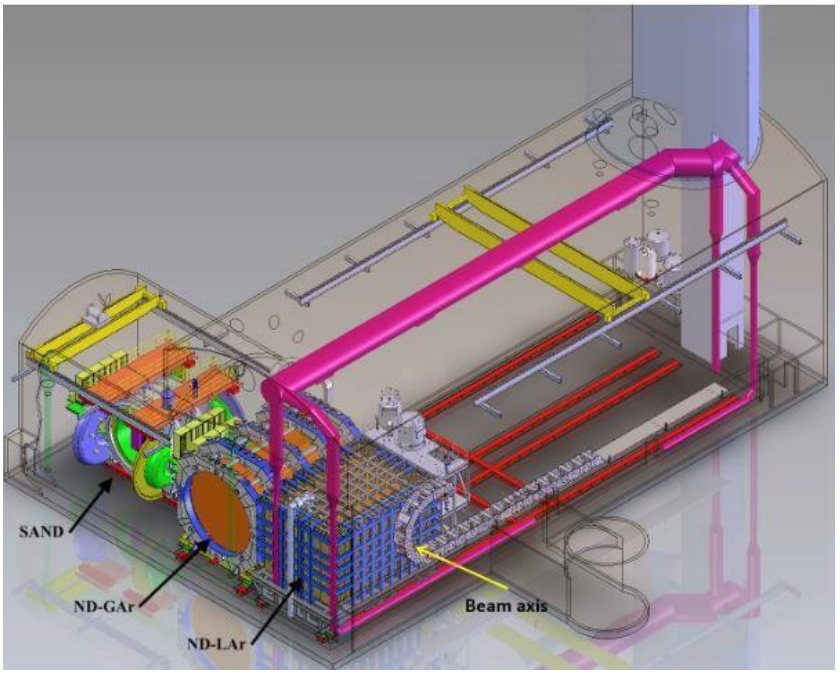

Figure 1.2: The components of the DUNE near detector complex: ND-LAr, ND-GAr and SAND [2].

ND-GAr will be a magnetised high-pressure gaseous argon-based Time Projection Chamber (TPC) surrounded by an electromagnetic calorimeter, in a 0.5 T magnetic field generated by superconducting coils. It is being designed to study neutrino-argon interactions, with argon being the medium to match the target nucleus of the far detector (the capabilities of gaseous versus liquid argon are described in section 1.2.2). The drift region will have a diameter and length of approximately 5 m each, giving a fiducial mass of almost 1 tonne of argon. With this volume, it is expected that 1.6 million interactions will be collected per year of operation. A schematic of ND-GAr is shown in figure 1.3 [2].

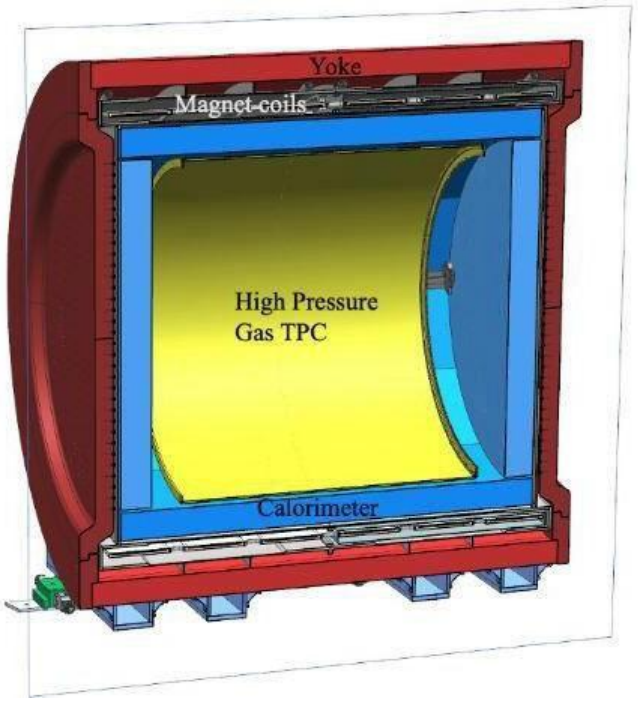

Figure 1.3: ND-GAr design, showing the high pressure gaseous region, the electromagnetic calorimeter and the magnetic coils.

1.2.2 Capabilities

An important role of ND-GAr will be to measure the momenta and sign of particles exiting from the upstream ND-LAr. Magnetisation from the superconducting solenoid will allow measurement of the momenta of muons, using the curvature in the magnetic field. By identifying the sign of charged particles, neutrino and antineutrino reactions will be distinguished.

One drawback of a gaseous medium is that a lower density than liquid argon would result in a low neutrino event rate. For this reason, the TPC will run at a pressure of 10 bar. An increased rate of neutrino interactions will produce a larger statistics sample. The lower density of gaseous argon compared to liquid argon (even at 10 bar) will provide a lower energy detection threshold, to enable reconstruction of pions, protons and nuclear fragments.

As ND-GAr will have a low detection threshold, it will be able to constrain nuclear effects in argon at the interaction vertex, which is one of the least understood uncertainties for neutrino oscillation analysis. Pions that are misidentified as knocked-out protons, or protons misidentified as pions, can be a cause for a significant misreconstruction of neutrino energies in the far detector and in ND-LAr. However, pions are rarely misidentified as protons in gaseous argon, and so ND-GAr will provide information on the frequency of this misclassification. Furthermore, secondary interactions occur at a far lower rate in gaseous argon when compared to liquid argon, due to the lower density of the medium. Confusion between primary and secondary particles is an important effect when reconstructing events from liquid argon TPCs, but this work focuses on a gaseous medium and therefore details of reconstruction techniques in liquid argon TPCs is not covered herein. However, a gaseous medium would evidently be beneficial in identifying those particles that are from primary interactions, due to the lower secondary interaction rate. These improved particle identification capabilities will enable the constraint of systematic uncertainties for neutrino oscillation analyses.

1.2.3 Light production and collection

A complete conceptual design for ND-GAr is still being developed, expected for the late 2020s with a final design in the early 2030s. To facilitate this final design, it is necessary to develop hardware prototypes, to carry out research and development tests. One major area of research and development for ND-GAr is light production and collection. A photon detection system in ND-GAr could enable the absolute determination of the interaction time in the TPC, by collecting primary scintillation light signals [3]. This would be a novel development for gaseous argon TPCs. The primary scintillation light could be collected by instrumenting the plane behind the TPC cathode with photosensors, and lining the field cage with a reflective material (Geant4 simulations of the light collection efficiency are

described in chapter 6). Secondary scintillation light signals could also be imaged with an optical readout method. An ongoing research effort is on the design of the photon detection system.

In pure gaseous argon at 10 bar, a minimum ionising particle would produce photons mainly in the vacuum ultraviolet (VUV) region, at 1400 photons/cm [4]. However, it is a typical requirement to add a quench gas to TPCs for stable operation, and quench gases absorb VUV photons. Doping argon gas with a small percentage of CF_4 quenches the gas mixture, with the added benefit of wavelength shifting photons from the VUV to the visible region [5], which increases the detection capabilities of the light.

1.3 Motives of this work

GAT0 is an optical TPC, being developed as a technology demonstrator and prototype for ND-GAr. This work demonstrates charge amplification with Gaseous Electron Multipliers (GEMs) and optical imaging of secondary scintillation in Ar:CF_4 gas using GAT0, as is an envisioned requirement to illustrate for ND-GAr. Absolute timing of neutrino interactions can be carried out by time-tagging the primary scintillation signal. However, the precision to which this can be achieved will be limited by the time resolution of the photosensors that are employed. The study of the timing capabilities of silicon photomultipliers (SiPMs) with combined channels in the frontend electronics readout board was experimentally tested and is described. Multiple readout channels need to be combined to enable large-area coverage, however this results in a degradation of the achievable time resolution. The time resolution can be characterised by measuring the signal-to-noise ratio and dark count rate of the SiPMs with their associated readout electronics. .Finally, Geant4 simulations of the light collection efficiency of the SiPMs with a PTFE reflective layer lining the field cage of the GAT0 TPC were carried out.

Chapter 2

Time Projection Chambers

2.1 Operating principles

The Time Projection Chamber (TPC) was first introduced in 1976 [6]. It consists of a gas-filled sensitive volume, with a cathode and anode. A particle passing through the gas volume excites and ionises atoms in the gas mixture along its trajectory. The cathode is biased with a high voltage, to supply a drift electric field. Electrons released from the ionisation travel under the influence of the drift field, towards the anode. At the anode, electrons can be collected and read out. Field-homogeneity in the drift region is provided by a field cage which surrounds the drift region, typically made from conducting rings, which divide the electric potential from the cathode. If a magnetic field is applied perpendicular to the electric field in the drift region, the momenta of passing particles can be determined by the curvature of their trajectories, caused by the Lorentz force. The basic concept of a TPC is illustrated in figure 2.1 [7].

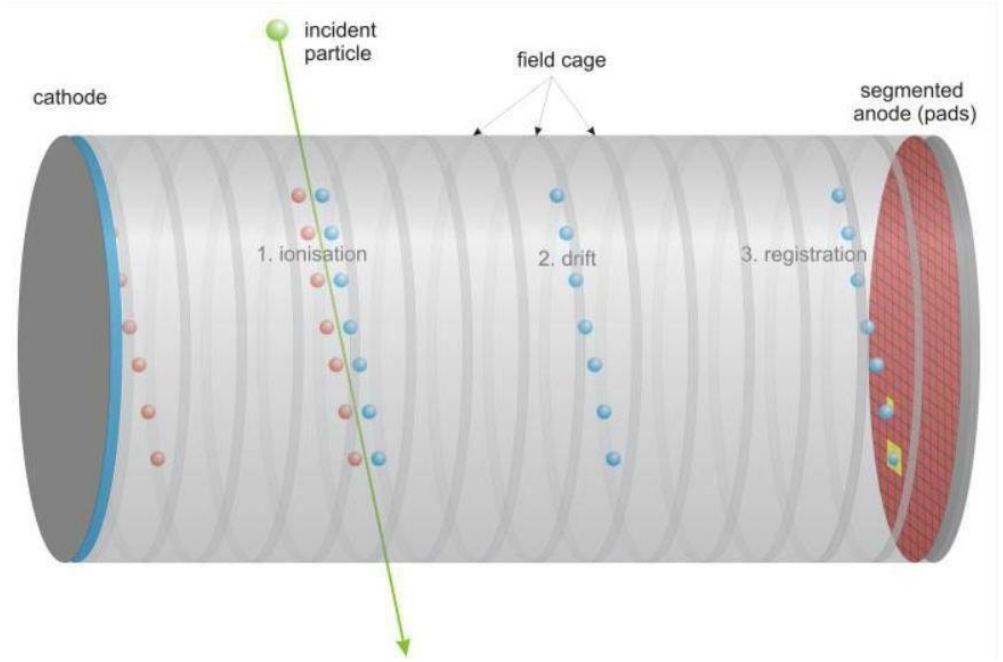

Figure 2.1: The structure of a basic TPC [7].

The x- and y-coordinate positions of a particles trajectory as it passes through the TPC gas volume can be obtained if the anode is segmented by pads, directly from the projection onto the anode. The z-coordinate can be obtained from the drift time, which is the time between the particle passing through the TPC volume and the associated anode signal. When particles pass through the TPC, alongside ionisation electrons they also produce scintillation light from excitation and subsequent deexcitation of the gas atoms and molecules. Sensors such as SiPMs can be used to record the time of the primary scintillation signal. To determine the distance between the interaction point and the anode, the drift velocity of the ionisation electrons is calculated. In this way, three-dimensional positional information can be reconstructed of the particles' trajectory.

2.2 Drift and diffusion

The average velocity of ionisation electrons in a gas can be described by the Maxwell-Boltzmann distribution, using the following equation [8]:

$$\langle v \rangle = \sqrt{\frac{8k_{\mathrm{B}}T}{\pi m}} \tag{2.1}$$

where k_B is the Boltzmann's constant 8.62×10^{-5} eV/K, T is the temperature of the gas and m is the mass of the particle under motion.

Under the influence of a TPC drift field, the ionisation electrons move towards the anode. Alongside moving towards the anode, they also undergo longitudinal and transverse diffusion, moving in a manner to reduce a density gradient between the electrons and the target gas. In the drift region, diffusion of the charges needs to be minimised to maintain high resolution of the particle tracks.

When drifting in a TPC filled with pure argon gas, the electrons mainly experience elastic scattering, and only a small fraction of the electron energy is transferred to the argon atoms. The electron energy dependence of ionisation, excitation and elastic scattering cross-sections in argon gas is shown in figure 2.2 [9]. When adding a molecular additive to the argon gas, new inelastic scattering energy transfer channels become available, offering lower energy levels in the form of vibrational and rotational states. These inelastic scattering processes have lower cross-sections than of elastic scattering, but still can transfer ~100 times more energy to the gas, therefore reducing the level of electron diffusion in the drift region [10].

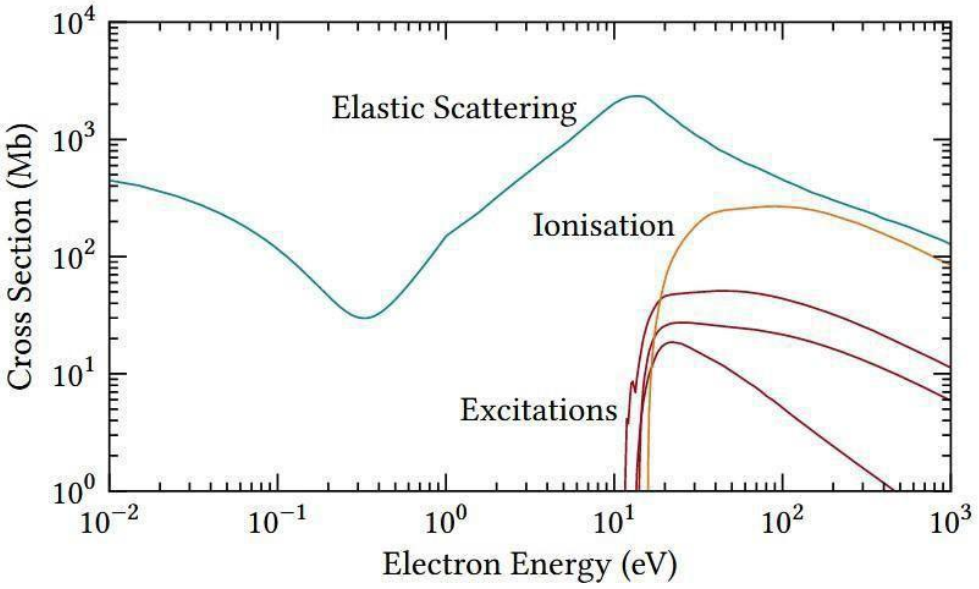

Figure 2.2: Electron energy cross-sections for elastic scattering, ionisation and excitation processes in argon gas [9].

2.3 Charge amplification with gaseous electron multipliers

Ionisation electrons produced in the initial interaction would typically produce a signal that would be too small to detect if they were not amplified before reaching the anode, due to their low quantity. Structures such as Gaseous Electron Multipliers (GEMs) [11] can be used to produce secondary ionisations, by means of avalancheprocesses.

A GEM consists of an insulating substrate, coated on either side with conducting electrodes. The structure is perforated with a dense matrix of micropatterned holes, as can be seen in the microscopic image in figure 2.3 [12]. Application of a suitable potential difference between the two electrodes produces regions of high electric field strength within the holes. Electrons entering the holes acquire sufficient energy to induce secondary ionisations, triggering an avalanche amplification process. The typical electric field within the holes is illustrated in figure 2.4 [12].

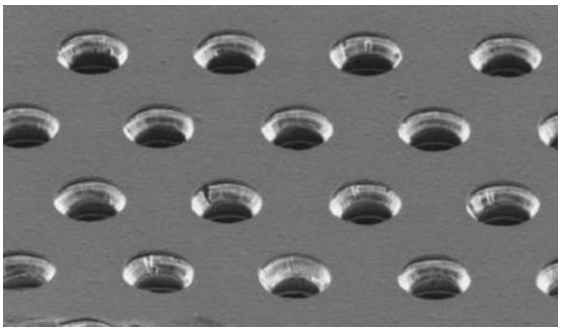

Figure 2.3: A microscopic image of GEM holes [12].

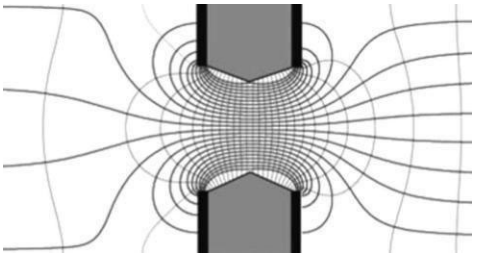

Figure 2.4: The electric field lines in a hole of a GEM [12].

Primary ionisation electrons produced in the drift region are accelerated to GEM holes with the applied drift electric field. Electrons gain kinetic energy due to acceleration from the high electric field within the holes, in between their collisions with the gas atoms. The mean free path, λ, is the average distance a primary electron travels between collisions, and provides the Townsend coefficient, α:

$$\alpha = \frac{1}{\lambda} \tag{2.2}$$

The Townsend coefficient thus depends on gas pressure and electric field strength. The number of secondary electrons, dN , produced per unit length during the avalanche process in the holes can be determined after a path length dx travelled by N primary electrons:

$$dN = N \,.\, \alpha \, dx \tag{2.3}$$

If N_0 primary electrons enter the holes of the GEMs, the detector gain, M , is characterised by the multiplication factor, where $N\,(x)$ is the number of electrons after path length x:

$$M = \frac{N\,(x)}{N_0} \tag{2.4}$$

The multiplication factor has a limit before discharges caused by electrical break-down. A phenomenological limit given by the Raether limit gives a maximum gain of $\sim\ 10^6$ [13]. Discharges can cause serious damage to the GEM structure, which can lower the achievable gain.

2.4 Quenching

Excitation and subsequent deexcitation of gas atoms following electron energy transfer results in the emission of photons in the vacuum ultraviolet (VUV) region. These photons undergo photoelectric interactions with the gas and produce secondary ionisation electrons. The secondary electrons can go on to further ionise, leading to a chain reaction which can destabilise the detector operation and produce discharges. Molecular quench gases added in small quantities can absorb the VUV photons to maintain a stable operation. However, if detection of the photons is necessary, for example to time-tag reactions, then a high-level of quenching will reduce the sought light yield.

2.5 Optical readout

2.5.1 Photosensor technology requirements

In an optical TPC, scintillation light produced is detected by installing photosensors. Depending on the purpose of imaging the scintillation light, the type of photosensor employed varies. Some photosensor properties that are considered include single photon detection capability, dark count rate, magnetic field compatibility, pressure rating, wavelength efficiency and sensitive area. Widely employed photosensor technologies in gaseous detectors are silicon photomultipliers (SiPMs), photomultiplier tubes (PMTs), CMOS and CCD cameras.

Detection of the primary scintillation light signal can be done to determine the initial time of interaction inside a TPC, as described in section 2.1. PMTs offer the single-photon sensitivity required, but are not rated for operation in a high magnetic field, nor at high pressures. In comparison, SiPMs can operate in a high magnetic field and at high pressures with single photon sensitivity. They also require lower operating voltages and have longer lifetimes [14]. However, SiPMs suffer from a high dark count rate at room temperature [15] and individually have small sensitive areas.

Primary ionisation electrons that are drifted to regions of high electric fields in amplifications structures such as GEMs can produce secondary scintillation light, as will be described in section 3.2. Detecting secondary scintillation light

can produce a 2-dimensional track image, with a projection of the trajectory of the ionising particle. This can be achieved by placing a CMOS or CCD camera after the amplification stage of a TPC.

It can be a requirement in TPCs to detect both the primary scintillation light for time-tagging, and the secondary scintillation light for 2-dimensional track imaging, by using two separate photosensors. In both cases, the wavelength efficiency of the photosensor used would need to match the wavelengths of the primary and secondary scintillation light emissions. However, if the emission is in the VUV region, then most photosensor technologies are not optimised for the detection of this light. This can be overcome by shifting the wavelength of the scintillation emissions to the visible region.

2.5.2 Silicon photomultipliers

Structure of a silicon photomultiplier

An SiPM is a solid-state photodetector, formed by connecting in parallel several identical small-sized cells that are fabricated on silicon. Each cell consists of a Geiger-mode avalanche photodiode (APD) in series with a quenching resistor. Geiger-mode APDs are capable of single-photon detection, but individually their signals do not contain information about the intensity of the incident light. By connecting several cells in parallel with a common-bias and common-cathode, this limitation is overcome. The basic design of an SiPM is shown in figure 2.5 [16].

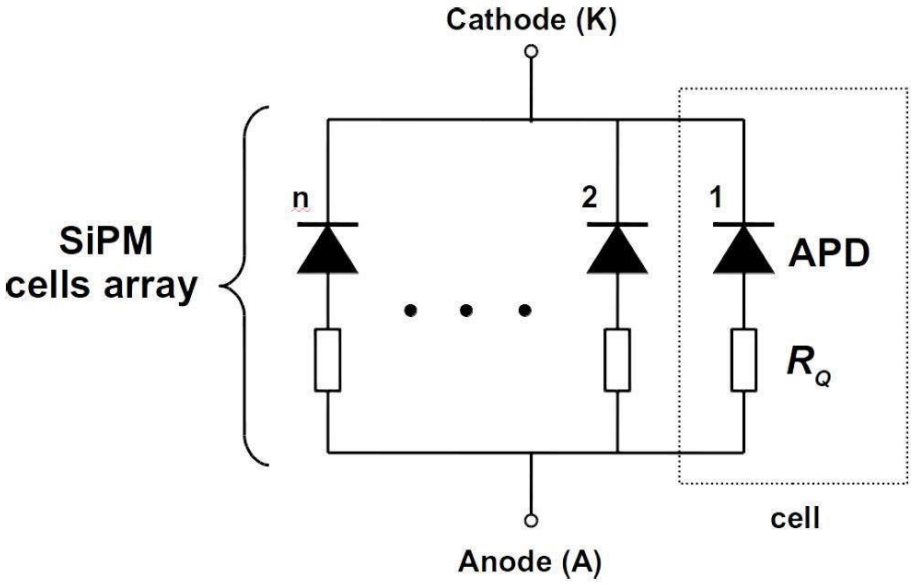

Figure 2.5: The composition of an SiPM, with multiple cells of quenching resistors and APDs in series. [16]

Geiger-mode operation

A Geiger-mode APD operates with the presence of an electric field region, that is created by an external reverse bias. A single photon incident on a cell can generate electron-hole pair charge carriers, which then roam with movements influenced by the electric field. If the electric field is increased by applying a higher reverse bias, the mean energy of the carriers can exceed a threshold, to produce impact ionization and release secondary charge carriers [17]. This can trigger an exponential charge amplification avalanche, rapidly increasing the number of charge carriers. When the electric field is high enough so that a single charge carrier triggers a

self-sustained avalanche, the APD is in Geiger mode, and the bias at which this occurs is referred to as the breakdown voltage. The avalanche is stopped when the current spike in the quenching resistor of the cell lowers the voltage on the APD, thus reducing the probability of impact ionization.

The APD makes use of avalanche charge multiplication as its' gain mechanism. The gain of the avalanche is the ratio of the total amount of charge that is collected and the fundamental electron charge, with a typical value in the range of 10^5 to 10^6. [14].

Photon counting

When a photon is incident on an APD, an output pulse is generated. A single cell in an SiPM can only detect a single photon at a time, and hence the measured output pulse amplitude from a single cell does not reveal information about the number of photons detected at one moment in time. However, if multiple cells in an SiPM absorb photons simultaneously, the resulting output pulse amplitude is

a superposition of the amplitudes from each cell. Hence, the signal amplitude has discrete heights which correspond to the number of detected photons, as seen in the oscilloscope traces in figure 2.6 [18]. For example, if two photons are incident on separate cells of an SiPM, the pulse amplitude is twice as high as the amplitude from one photon. Using this knowledge, it is possible to count the number of

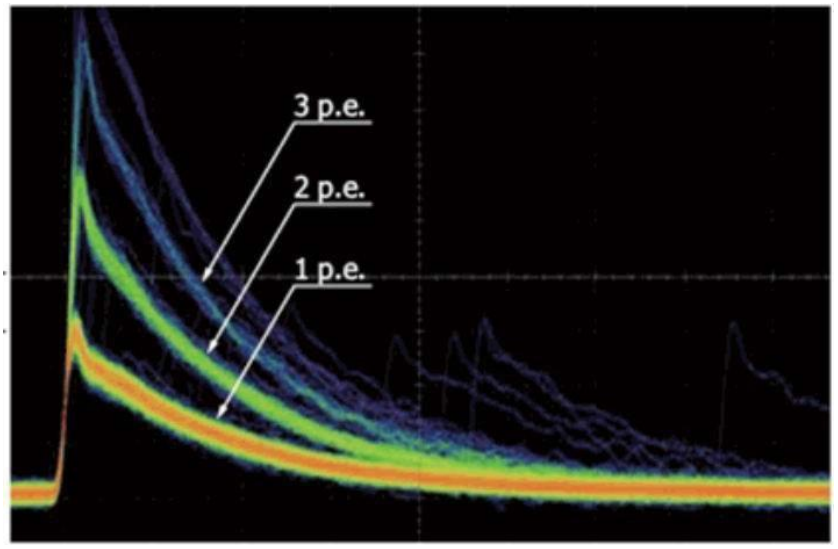

Figure 2.6: Ocillscope traces showing discrete photon bands [14].

photons that were incident on the SiPM, by analysing the output pulse heights, and thus determine the gain of the SiPM [14].

Chapter 3

Interactions with matter

3.1 Charged particles

Charged particles interact with matter through electrostatic forces. Depending on the amount of energy a charged particle transfers in an interaction, either ionisation or excitation of atoms and molecules in the medium can occur. The mean energy lost per unit length of a charged particle with velocity v, charge z and energy E interacting with matter, when it travels a distance x into matter of electron density n and mean excitation energy I, is provided by the following Bethe-Bloch formula [19]

$$-\left\langle \frac{dE}{dx} \right\rangle = \frac{4\pi}{m_e c^2} \cdot \frac{nz^2}{\beta^2} \cdot \left(\frac{e^2}{4\pi\varepsilon_0} \right)^2 \cdot \left[\ln \left(\frac{2m_e c^2 \beta^2}{I \cdot (1-\beta^2)} \right) - \beta^2 \right] \qquad (3.1)$$

Here $\beta = v/c$, and e and m_e are the charge and mass of an electron respectively.

The energy lost by a charged particle when it ionises a target medium to produce a single electron-ion per is called the W-value. The W-value is higher than the ionisation energy of the target medium, as some energy is also transferred in exciting atomic electrons to higher bound states. The W-value of pure argon for 5.31 MeV alpha particles is 26.31 eV [20].

The number of ionisation events, N, can be obtained by dividing the energy transferred by the charged particle, E, by the W-value, W:

$$N = \frac{E}{W} \tag{3.2}$$

However, the amount of electron-ion pairs created by a charged particle is a statistically fluctuating process, following a Poisson model distribution. The total number of ionising collisions, N_I , along a distance x travelled by the particle is given by:

$$N_I = \frac{x}{n \times \sigma^{-} - 1} \tag{3.3}$$

where n is the number density of the medium and σ is its cross-section [21].

If the energy transferred by the charged particle is less than the ionising energy of the medium, then excitation of atoms and molecules in the medium can occur.

3.2 Photons

Photons emitted from excitation and subsequent deexcitation interact with matter via the photoelectric effect, Compton scattering or pair production. The attenuation of photons, $I(x)$, after they travel a distance x can be described by the following expression:

$$I(x) = I_0 \mathrm{e}^{-\mu x} \tag{3.4}$$

where I_0 is the initial intensity of the photons and μ is the attenuation coeeficient. Unlike charged particles that gradually loose energy as they travel through matter, photons are attenuated through either absorption or deflection. The photon interaction cross-section for each process depends on the atomic number of the target medium and the photon energy, as is illustrated in figure 3.1 [22].

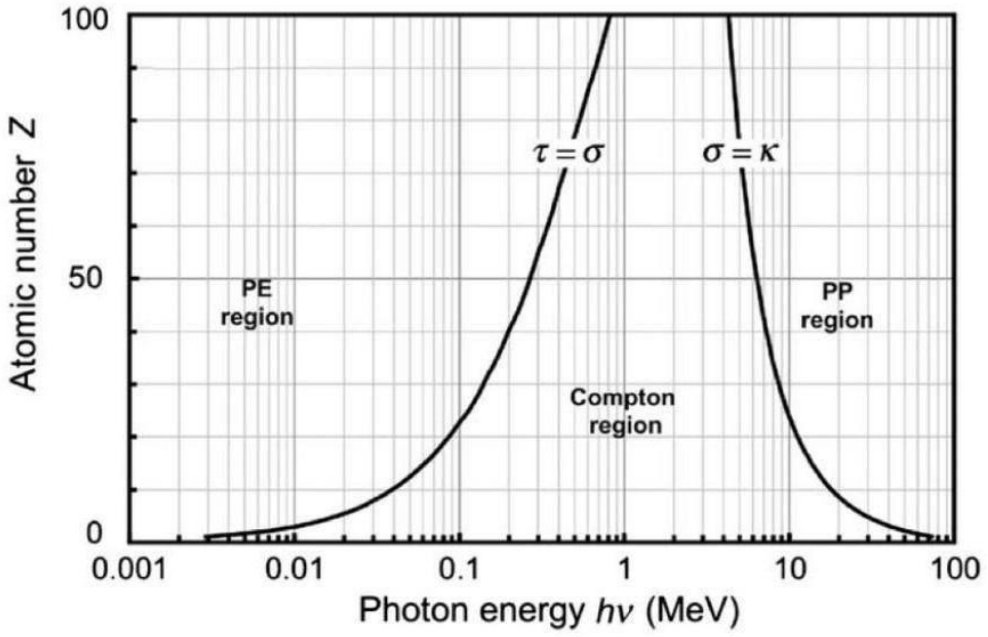

Figure 3.1: Cross-sections for the photoelectric effect, Compton scattering and pair production as a function of photon energy, for target mediums of different atomic numbers [22].

3.2.1 The photoelectric effect

The photoelectric effect occurs for photons of lower energies. When a photon is absorbed by an orbital electron, the electron can acquire sufficient energy to be

ejected from the atom. An electron from an outer shell replaces the electron, and in doing so emits a photon of a characteristic energy. The energy of the emitted photoelectron, E, is given by:

$$E = E_p - E_B \tag{3.5}$$

Where E_p is the photon energy and E_b is the binding energy of the electron. The recoil momentum of the electron caused by photon absorption is absorbed by the nucleus.

For a fixed photon energy, the absorption cross-section increases with higher atomic numbers of the target medium. The photon absorption cross-sections in argon as a function of photon energies is shown in figure 3.2 [23]. Photons which have an energy which is close to the binding energy of an electron have an increased probability of interaction. For example, the photon cross-section is small at photon energies which are above the highest binding energy of the atom, the innermost K-shell, but it increases as it reaches the K-shell energy. The K absorption edge, 3.2 keV for argon, is where the cross-section drops rapidly, as the electrons in the K-shell do not undergo the photoelectric effect. The figure shows similar L and M absorption edges.

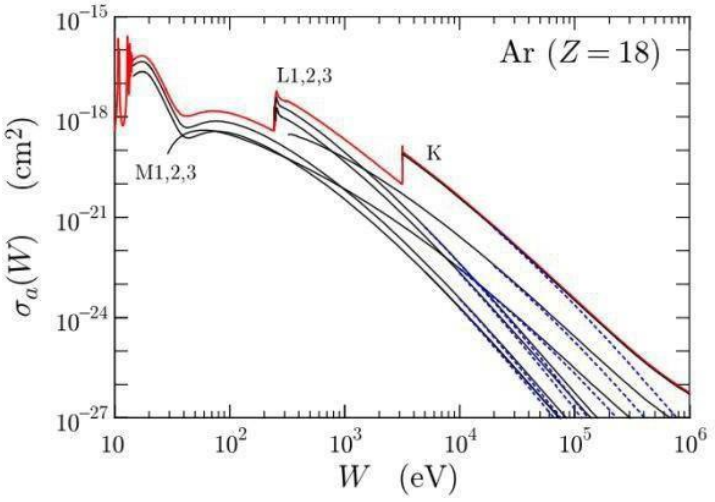

Figure 3.2: Cross-sections for photon absorption by argon atoms as a function of

photon energy, displaying the K, L and M absorption edges. The red line shows total atomic cross-section and the blue lines are from dipole approximations [23].

If the incident photon has a sufficiently high energy to be absorbed by an inner shell electron, a characteristic X-ray photon with an energy corresponding the quantised atomic orbital energy levels is emitted and reabsorbed instantaneously.

3.2.2 The Compton effect

The Compton effect occurs when a photon undergoes inelastic scattering off an electron in an outer shell. The electron binding energy can be neglected if the energy of the incident photon, Ep, is sufficiently high, so the electron undergoes inelastic scattering with the photon as though it were a free electron. Energy transfer from the interaction causes ejection of the electron, with the resulting

energy, Ep', and scattering angle, θ, of the photon being given by [24]:

$$E_{\gamma'} = \frac{E_\gamma}{1 + \frac{E_\gamma}{m_e c^2}(1 - \cos\theta)} \tag{3.6}$$

3.2.3 Pair production

In pair production, an incident photon is converted into an electron-positron pair. The photon energy must be greater than the rest mass of the electron-positron pair, for this process to occur. Pair production typically occurs within the electric field if an atomic nucleus, which absorbs the recoil energy for momentum conservation.

3.2.4 Primary and secondary scintillation

When a charged particle interacts with a medium, alongside the production of primary ionisation electrons, it leads to excited states of atoms and molecules in the medium. Photons emitted following de-excitation are referred to as primary scintillation light. If primary ionisation electrons are drifted to a high electric field region, such as to a GEM-like amplification structure, they can themselves produce further ionisation and excitation events. This leads to the production of secondary scintillation light, called electroluminescence light.

The excited states of the medium evolve with time through chemical reactions, and eventually reach an intermediate state that decays and gives a characteristic scintillation spectrum, showing the energies of the emitted photons. By knowing the decay probability and state-to-state transition probabilities, the time evolution of the excited states could have been calculated to obtain the scintillation spectrum, were it not for the role of the chemical reactions. Chemical reactions result in several energy levels and species, with numerous possible competing interactions between each of them. Scintillation spectra as a result have bands and peaks from dimers, ions and atomic levels, and they cannot be computed directly. Some example chemical reactions are presented below, in which a noble gas medium is

referred to as NG and an additive as AB [10].

$NG^* + AB \rightarrow NG + AB^*$ Wavelength-shifting

$NG^* + AB \rightarrow NG + A + B$ Molecular dissociation

$NG^{**} + NG \rightarrow NG^* + NG$ Self-quenching

$NG_2^*(v \neq 0) + NG \rightarrow NG_2^*(v = 0) + NG$ Excimer relaxation

$NG_2^*(v = 0) \rightarrow NG_2(v = 0) + NG + h\nu$ Excimer emission

3.3 Scintillation in Ar:CF_4 gas mixtures

Often it is the case that molecular additives are added to scintillating noble gas mediums for detector operation, to exploit certain properties. For example, as described in chapter 2.4, quenching components are added in small proportions to absorb highly-energetic VUV photons which can destabilise detector operation. However, in doing so, the scintillation light yield is reduced, which is a disadvantageous side-effect.

Despite this, one further motivation for adding a molecular additive is to reduce diffusion of ionisation electrons in the detector gas. This is achieved through a process called electron cooling, whereby ionisation electrons loose energy to the molecular components after inelastic scatterings, due to the latter's vibrational

and rotational degrees of freedom.

Furthermore, adding a molecular additive can result in wavelength-shifting of the scintillation light yield due to energy transfer reactions, as described in the previous section. If the wavelength-shifting can occur from the VUV region to the visible or near infra-red region, then the scintillation yield would be in a region where light detection would be easier, as readily-available commercial photosensor technologies can be used. The added benefit would be that the detector gas will still be quenched for stability.

A study [25]has shown that by doping argon gas with molecular CF_4, wavelength shifting of scintillation light occurs to a band centred at $\lambda = 630$ nm.

As the visible light is easier to detect than VUV light, it is not disadvantageous for the gas mixture to quench the highly-energetic VUV photons. Therefore, quenching for detector stability does not come at a cost of reduced beneficial scintillation yield. Figure 3.3 [25] displays a kinematic scheme showing the various transfer, decays and quenching reactions responsible for the wavelength shifting in Ar:CF_4. Scintillation yield spectra in the gaseous pressure range of 1–5 bar and CF_4 concentrations from 0.1% to 10% are shown in figure 3.4 [25]. The transmissions begin to occur with as little as 0.1% of CF_4 added to the mixture. The integrated yields shown in different bands as a function of the percentage concentration of CF_4 are shown in figure 3.5 [25]. The visible band (400 nm – 700 nm) has the highest yield with 1% of CF_4.

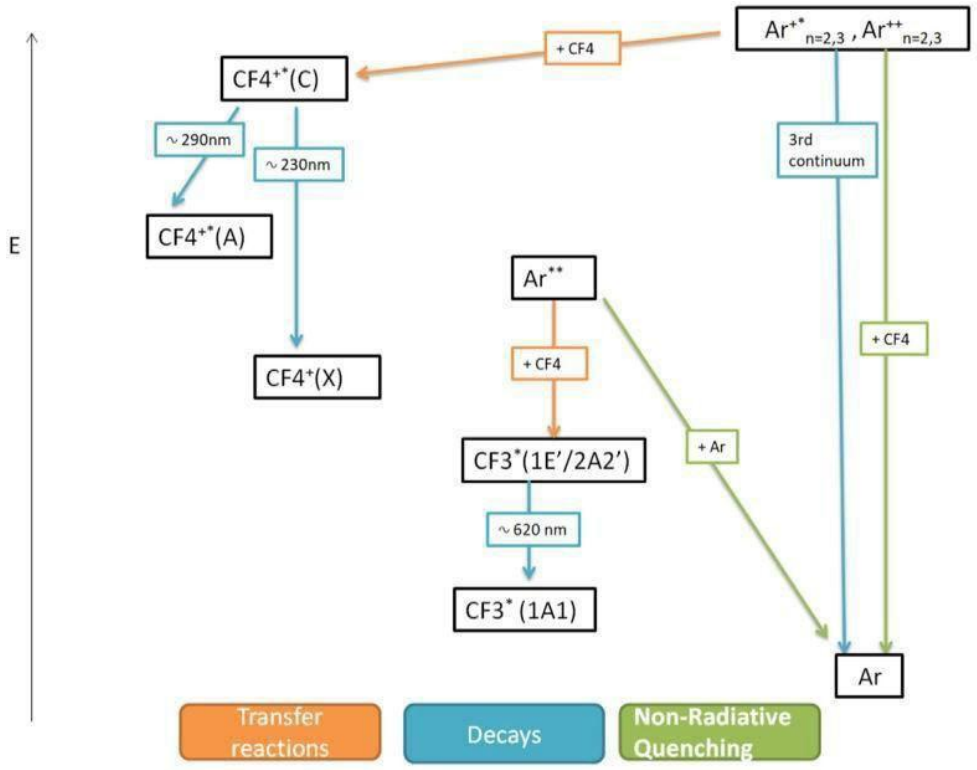

Figure 3.3: A kinematic scheme showing the transfer, decay and quenching reactions responsible for wavelength shifting in Ar:CF_4 gas mixtures [25].

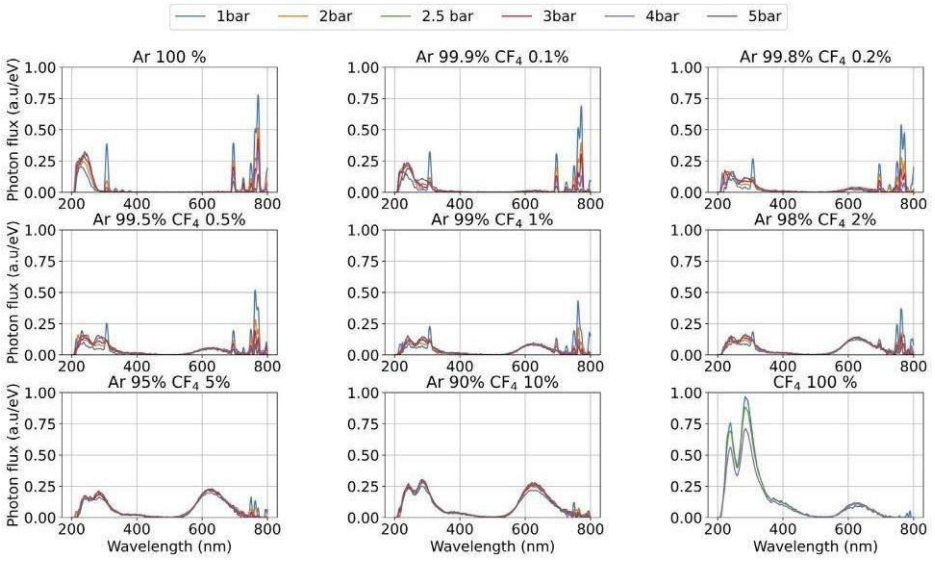

Figure 3.4: Scintillation emission spectra for different concentrations of CF4 doping in argon [25].

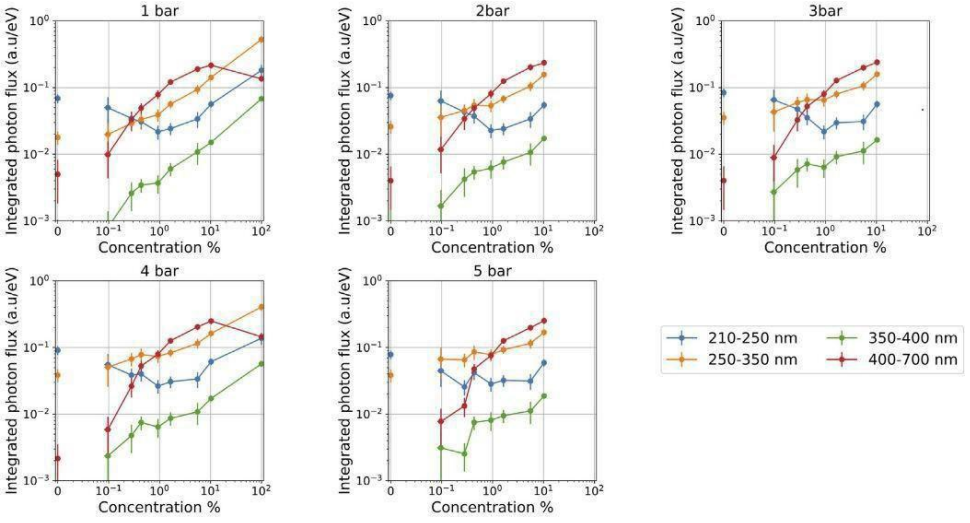

Figure 3.5: Integrated scintillation yields for different concentrations of CF4 doping in argon, shown in the different emission bands [25].

Chapter 4

The GAT0 optical Time Projection Chamber

4.1 Concept and geometry

GAT0 is an optical Time Projection Chamber, a prototype of the DUNE ND-GAr detector being developed to demonstrate interaction time tagging using primary scintillation and track imaging using secondary scintillation. A detector gas mixture of Ar:CF_4 with a ratio of 99:1 is chosen to have the same argon target nucleus as ND-GAr, whilst shifting the emission of the scintillation light from the VUV to the visible region and simultaneously quenching the highly energetic destabilising photons, as described in the previous chapter. It is necessary to keep the concentration of the CF_4 molecular additive as low as possible, to minimise the occurrence of non-argon parasitic reactions.

The main components of GAT0 are a field cage, a PTFE reflector, two GEM amplification structures, photosensors for time tagging and a CCD camera for track imaging. A diagram of GAT0 is shown in figure 4.1.

SiPM photosensors placed behind the cathode plane, where indicated in figure ??, will detect the primary scintillation light to enable time tagging of interactions

in a future upgrade, the development of which will be detailed in chapter 5. The field cage is made from a series of copper rings connected in series with resistors to homogenise the drift field, as shown in figure 4.2. The field cage is surrounded by a hollow cylinder made from the chemical polymer polytetrafluoroethylene (PTFE) [26]. PTFE is used as an electrical insulator, and also as a light reflector so that the primary scintillation light collection efficiency is maximised. Geant4 simulations of the light collection efficiency will be covered in chapter 6.

A drift field accelerates ionization electrons to a stack of two thick GEMs. Stacking two GEMs allows for two stages of amplification, giving an increased number of ionisation events and thus higher light yields. The first thick GEM is made from an acrylic substrate of 0.7 mm thickness, coated with copper on either side. The structure is perforated with holes of 0.7 mm diameter and 1 mm pitch. The second thick GEM is made from an FR4 substrate of 0.5 mm thickness, perforated with holes of 0.3 mm diameter and 0.5 mm pitch. A microscopic image of the acrylic thick GEM holes is shown in figure 4.3. The GEMs were placed in a holder, with a gap of 5 mm between them, as seen in figures 4.4 and 4.5. The GEM holder was placed on top of the field cage and the field cage was then mounted to inside the vessel, shown in figure 4.6. The assembled TPC after it was sealed with flanges is shown in figure 4.7.

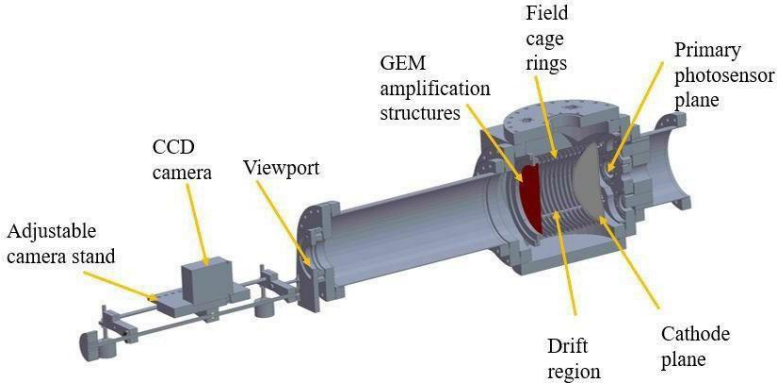

Figure 4.1: A diagram of the GAT0 optical Time projection chamber, labelling the key components.

Figure 4.2: The field cage, surrounded on the inner side with a PTFE reflector

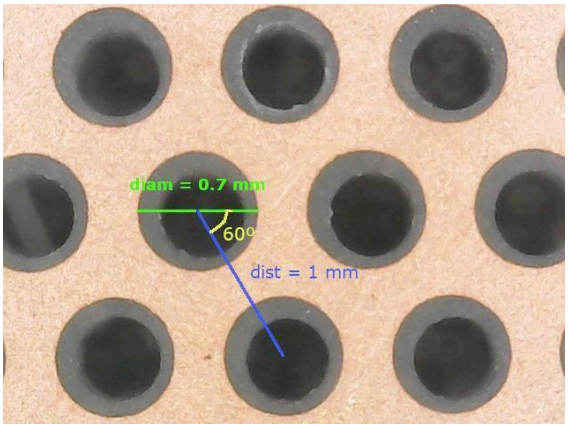

Figure 4.3: A microscopic image of holes in the acrylic thick GEM.

Figure 4.4: The acrylic thick GEM in a holder.

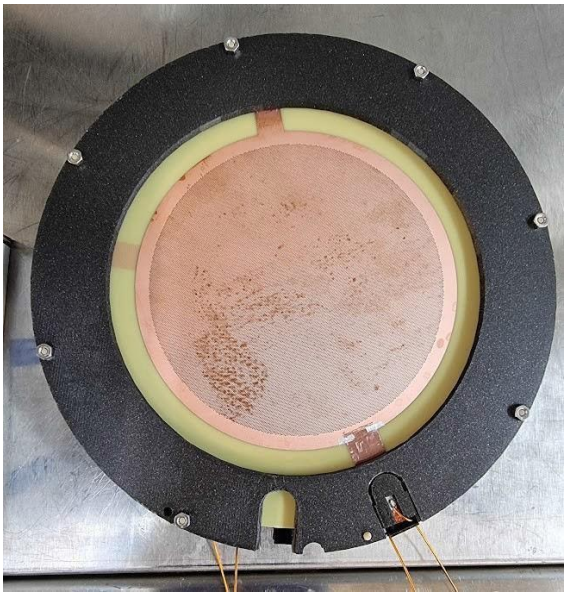

Figure 4.5: The FR4 thick GEM in a holder.

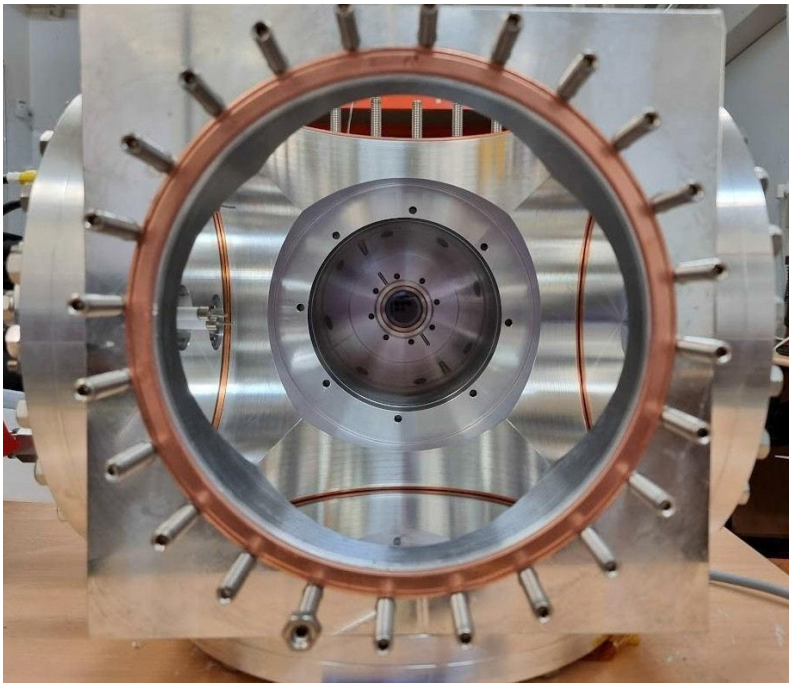

Figure 4.6: The empty vessel of the GAT0 optical TPC, prior to the field cage being mounted inside.

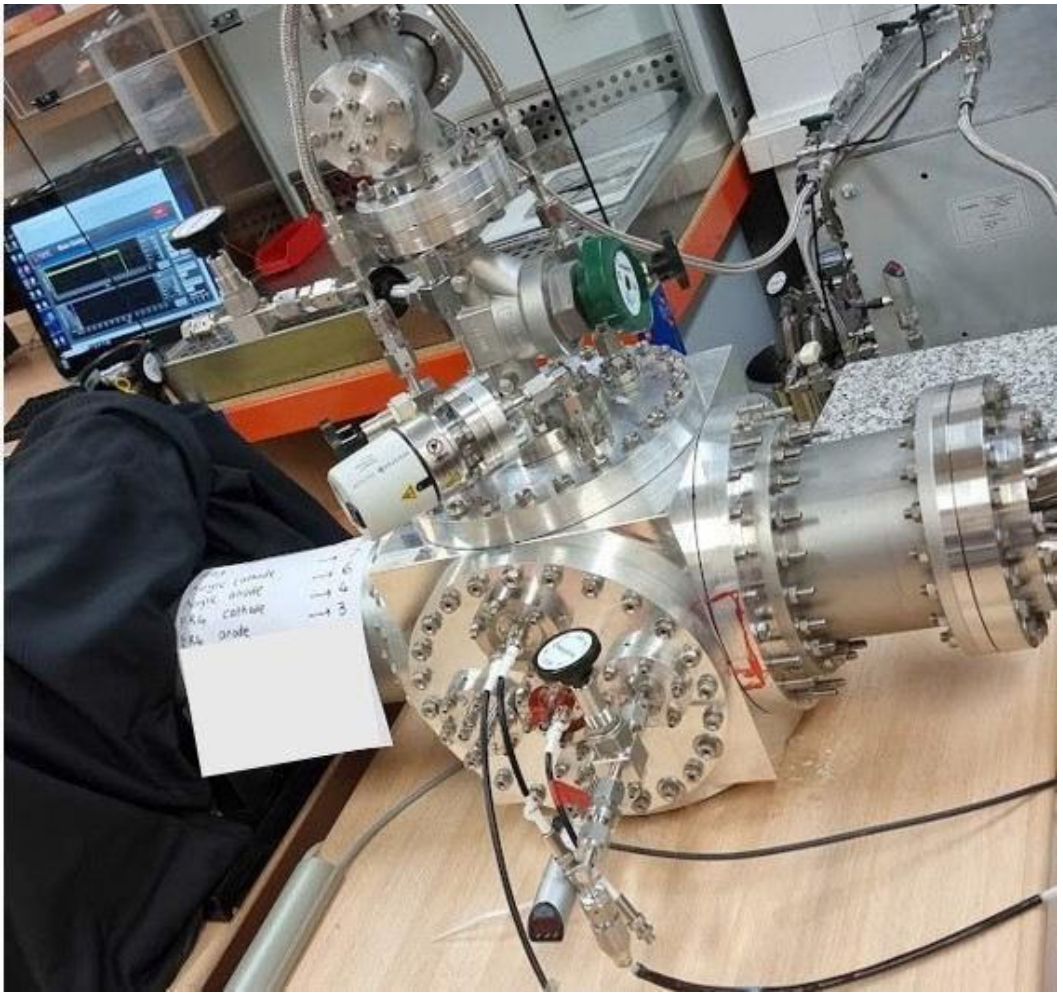

Figure 4.7: The assembled GAT0 optical TPC.

4.2 Alpha particle track imaging

After sealing the vessel, it was filled with 1 bar of Ar:CF_4 with a ratio of 99:1. Alpha particles from an americium-241 (Am-241) source placed within the TPC produced primary ionisation electrons. A drift field of 80 V/cm was applied by biasing the cathode and the top ring of the field cage, using CAEN high voltage modules. This drifted the primary ionisation electrons to the two stacked GEMs. The upper and lower copper conducting surfaces of both GEMs were also biased with CAEN high voltage modules, to potential differences of 1950 V and 990 V across the acrylic GEM and FR4 GEM respectively. This created high electric fields within the holes of the GEMs, leading to Townsend avalanches that produced secondary scintillation light, as described in chapter 3. The amount of secondary scintillation light produced was sufficient to allow the alpha particle ionisation

tracks to be imaged.

The imaging was done using a Retiga R6 CCD camera [27] with a quantum efficiency of 75% in the 400 – 1000 nm wavelength range, placed in front of the viewport as shown in figure 4.8 at a distance of ~520 mm from the surface of the upper (FR4) GEM, and surrounded with a light-tight enclosure to prevent ambient light contamination. The camera resolution was 224x183 pixels (width x height), and produced 16-bit output images with a 2 ms exposure time set per image. Each physical pixel of the camera was 4.54 μm x 4.54 μm, with a readout noise of 5.7 electrons. It was set to 8x8 binning, which combined 64 pixels into a single larger pixel. Binning provided a higher signal-to-noise ratio, as the noise remained at 5.7 electrons per bin.

Figure 4.8: The Retiga R6 CCD camera, in position in front of the viewport.

Images of secondary scintillation light from the alpha particle tracks are shown in figure 4.9. Am-241 undergoes primarily alpha-decay to neptunium-237 with a rate of ~200 Hz and a half-life of 432.6 years [28]. 85.2% of the decays produce alpha particles of 5.486 MeV, and 12.8% of 5.443 MeV. The decay scheme is shown in figure 4.10 [29].

This demonstrated for the first time the imaging of secondary scintillation with a double GEM stack, in the GAT0 prototype. This was achieved by shifting the wavelength of the light from the VUV to the visible region, using an Ar:CF_4

99:1 gas mixture at 1 bar. Future work will pressurise the TPC to up to 5 bar to assess if sufficient scintillation light is produced at high pressures to allow track imaging, as is a requirement for the ND-GAr detector.

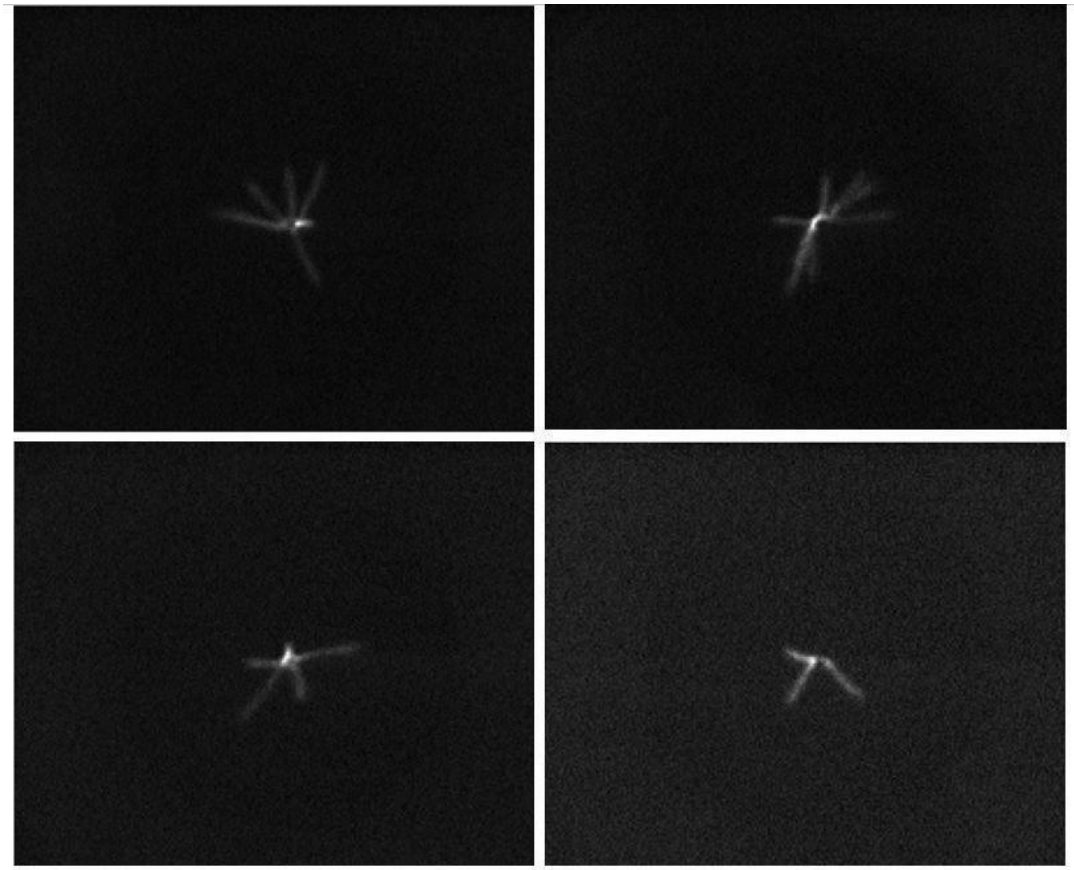

Figure 4.9: Images of alpha particle tracks from the GAT0 optical TPC.

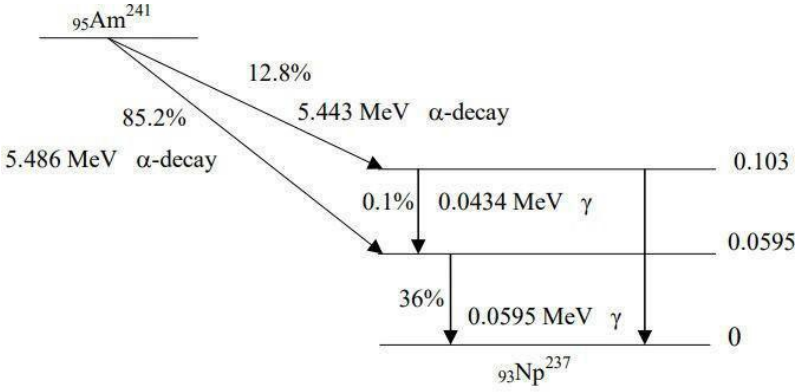

Figure 4.10: The decay scheme of Am-241 [29].

Chapter 5

Silicon photomultipliers (SiPMs) for primary scintillation detection

In the ND-GAr detector, the primary scintillation signal will be used to determine the absolute timing of neutrino interactions, with single-photon level sensitivity. The time resolution of the photosensor limits how precisely this information can be retrieved. The GAT0 prototype of the ND-GAR detector, described in the previous chapter, needs to be instrumented with a plane of SiPMs to detect the primary scintillation light.

ND-GAr is proposed to be in a magnetic field of 0.5 T [2] and operated at a high-pressure of 10 bar. SiPMs were thus proposed as a photosensor technology for the GAT0 prototype, and ultimately ND-GAr. SiPMs can operate at high-pressure and high-magnetic fields. PMTs are another photosensor technology, but they are not compatible for use in high-magnetic fields environments, nor are they rated for high-pressure. In comparison to SiPMs, PMTs also require higher voltages, and have shorter lifespans [14].

5.1 Requirements

5.1.1 Ganging

Individual SiPMs have a small surface area, which is not adequate for large-area coverage. To facilitate a larger detection area, multiple SiPMs would need to be installed. This would greatly increase the number of readout channels, giving rise to challenges related to power consumption constraints, noise from cables, data bandwidth and physical space limitations.

In order to overcome this challenge and achieve a large primary scintillation detection coverage area with multiple SiPMs, the readout channels from each SiPM can be combined into one readout channel. This is referred to as ‘ganging’ of channels in the readout front-end electronics.

5.1.2 Time resolution

A key requirement is having a high precision in the time resolution in the determination of the primary scintillation signal, whilst ganging several readout channels in the front-end readout electronics to enable a large-area SiPM coverage.

The SiPM time resolution is limited by the electronic response of the front-end readout electronics. Ganging several SiPMs into one readout channel increases the total capacitance [30]. A high parasitic capacitance in readout electronics degrades the time resolution by resulting in a slower rising edge of the signal caused by a higher slew rate (dV/dt), and also lowers the output pulse amplitudes [31]. The resulting reduction of the signal-to-noise ratio [32] will limit the time resolution, if a leading-edge threshold is used as a trigger method. A signal-to-noise ratio of 5-10 would allow nanosecond time resolution [3], and so one motivation of this study was to demonstrate if this level could be met.

Furthermore, SiPMs suffer from high dark count rates at room temperature [15], resulting from thermally generated charge carriers [17]. A high dark count rate increases baseline fluctuations in the waveforms, which also introduces fluctuations into the trigger threshold-crossing time, [31] degrading the time resolution. It is therefore important to measure and reduce the rate of these thermally generated

dark counts. Lowering the temperature reduces the dark count rate of the SiPMs [18] [15], and so a measurement of the dark count rate as a function of temperature was carried out.

5.2 Parallel ganging readout board for the silicon photomultiplier tile

The Hamamatsu S14161-6050HS-04 tile [33] consisting of an 25 cm^2 array of 4x4 SiPMs was selected as a prospective tile for the GAT0 prototype. A schematic of the SiPM tile with dimensions is shown in figure 5.1 [33].

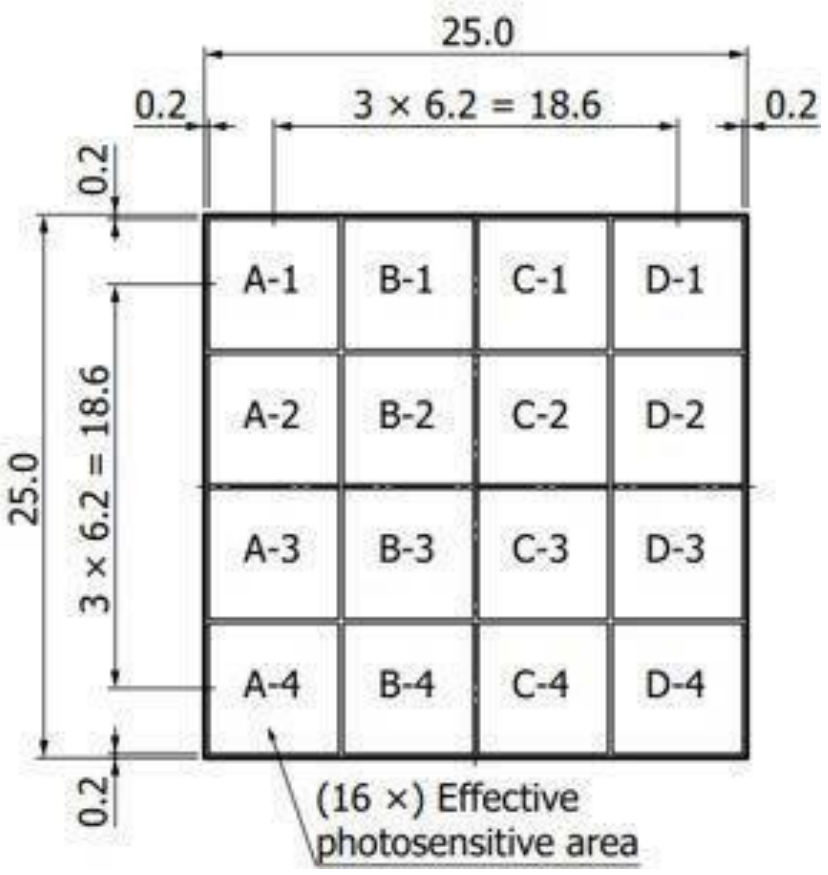

Figure 5.1: A schematic of the Hamamatsu S14161-6050HS-04 tile [33].

A readout board that ganged the 16 channels from each SiPM in the tile into a single output was designed for the amplification stage. The ganging scheme is

shown in figure 5.2. The transimpedance amplifier took a current input and

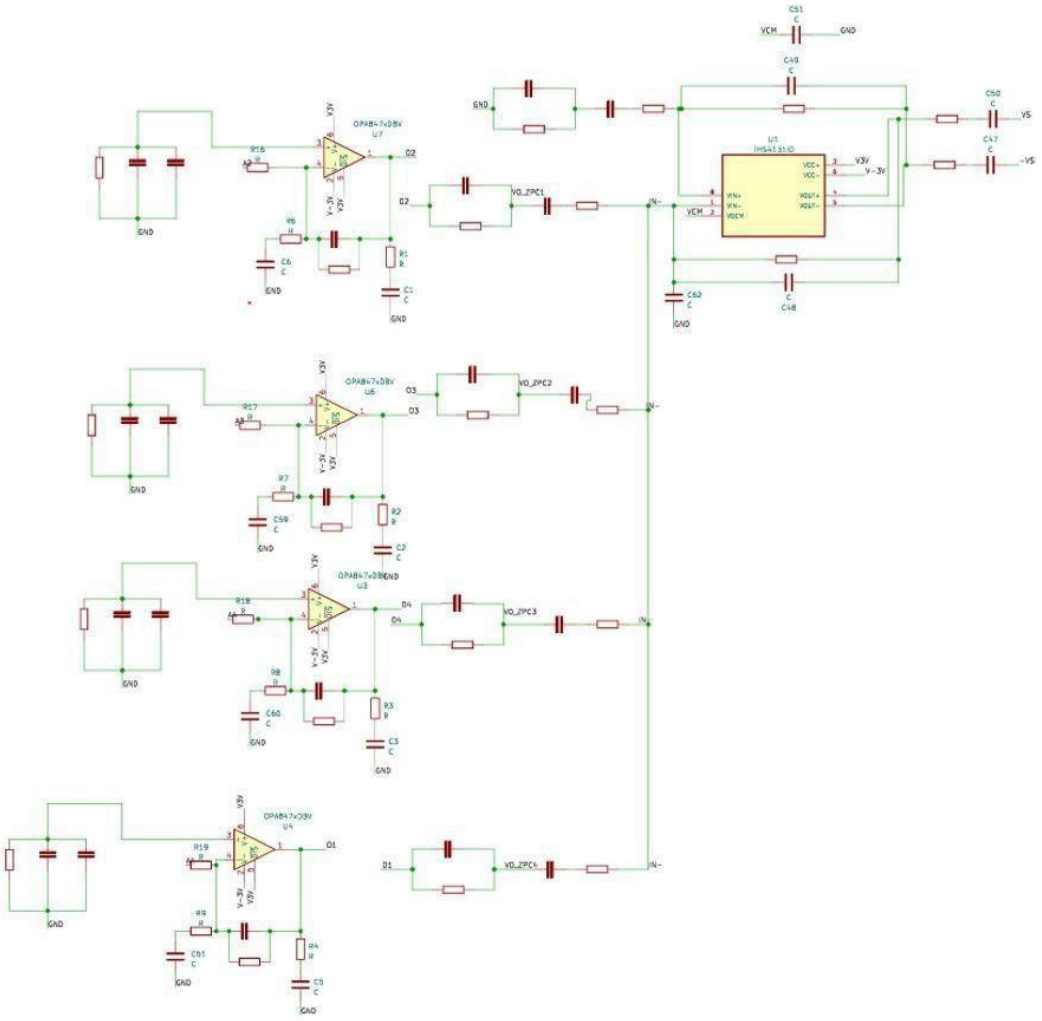

Figure 5.2: The electronic circuit diagram for the ganging of 16 signal outputs into one readout channel.

voltage output, with operational amplifier OPA847 that has a gain of 10^4 [34]. At the input of the transimpedance stage, there is parallel passive ganging of the SiPMs into four groups of four. An active ganging summing stage follows the passive ganging stage, with all the channels combined and readout with a THS4131 differential output amplifier [35]. The amplification readout board is shown in figure 5.3.

The SiPM tile was coupled to the amplification board and mounted on a power motherboard (figure 5.4), as is shown in figure 5.5.

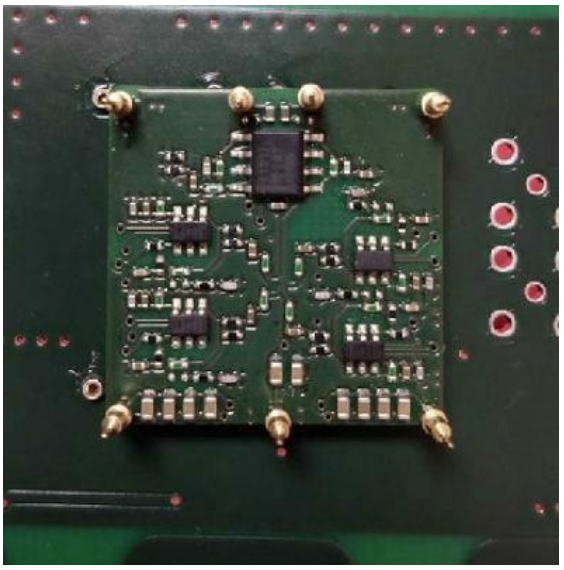

Figure 5.3: The printed circuit board of the amplification stage with the ganging of 16 channels.

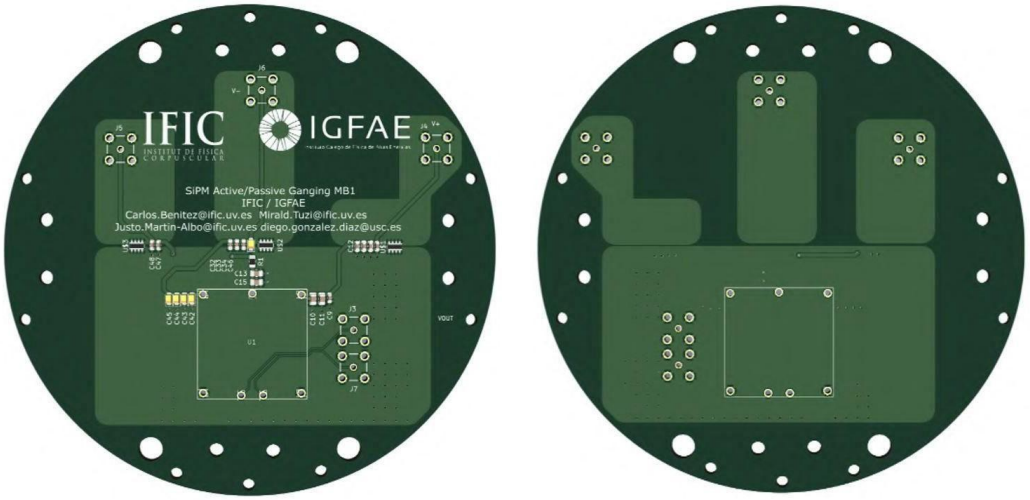

Figure 5.4: The two surfaces of the power motherboard, used for the amplification stage.

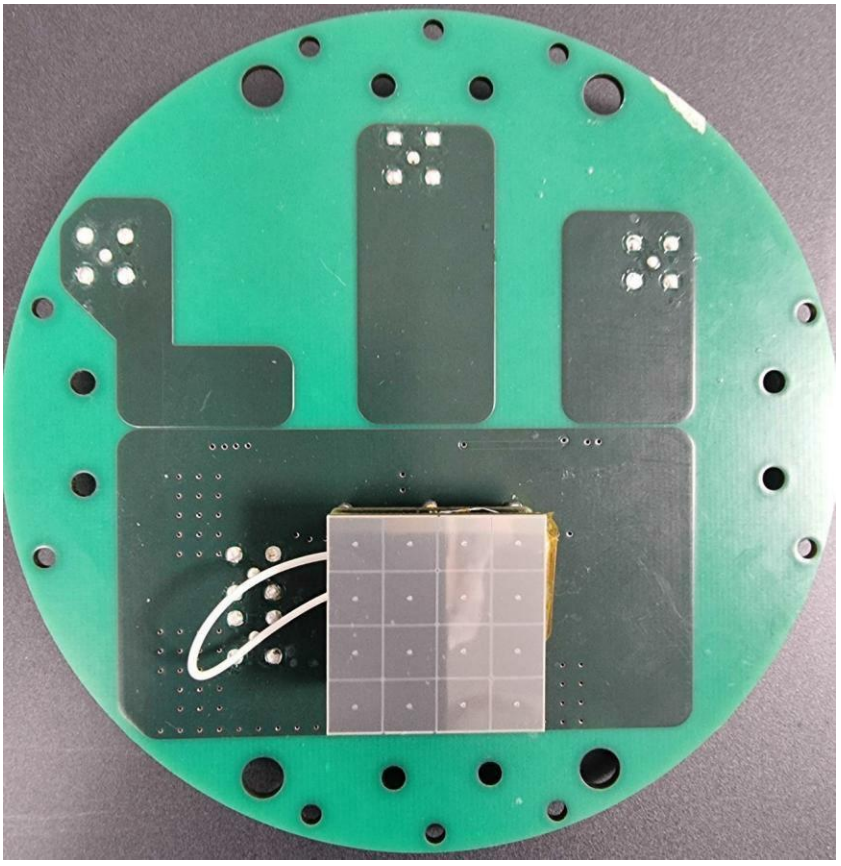

Figure 5.5: The SiPM tile mounted on the amplification stage, coupled to the power motherboard.

5.3 Experimental setup

In order to measure the gain, signal risetime, signal-to-noise ratio and dark count rate, an experimental setup that was temperature-controlled via liquid nitrogen was used, as illustrated schematically in figure 5.6. Dark count rates were mea-

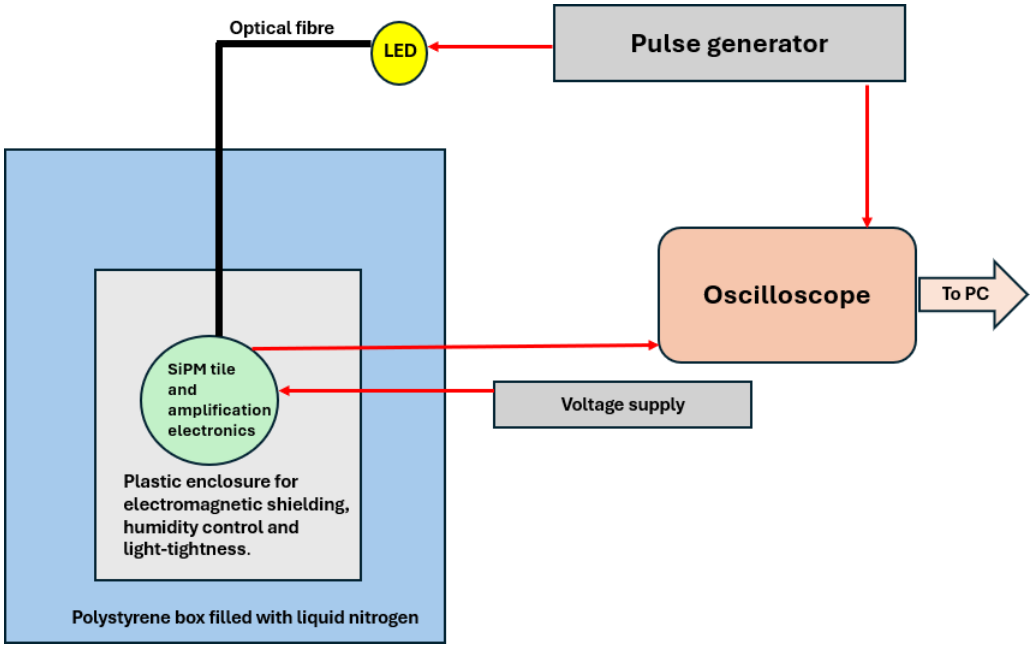

Figure 5.6: A schematic showing the experimental setup for the measurements of the SiPM tile and readout electronics.

sured at a range of temperatures from -35 ˚C to -10 ˚C, and the gain was measured at -35 ˚C so that the dark count rate would be minimised.

To achieve optical isolation, electrical insulation, and humidity control, the SiPM tile coupled to the readout board was mounted on a cylindrical hollow plastic enclosure, with the sensor facing inward (5.7). This was then placed in a secondary insulating plastic container that was partially coated with aluminium foil, for an additional layer of protection. The entire setup was placed in a thermally insulated polystyrene box (5.8), which was filled with a few centimetres of liquid nitrogen for cooling and then sealed. A temperature probe placed in close vicinity to the SiPM tile inside the plastic cylinder monitored the local temperature.

SiPMs operate at a few volts above the breakdown voltage of the APDs, referred to as their overvoltage. A Keithley 487 high voltage source unit was used to reverse-bias the SiPM with an overvoltage of 3 V. The amplification board was biased to +5 V, with a HMP4040 Rohde and Schwarz low voltage supply.

The output current pulses from the SiPM tile were converted to voltage signals in the transimpedance amplifier stage of the amplification board, and fed out from the polystyrene box into a room temperature environment. The signal was acquired directly by a Tektronix MSO44 oscilloscope, with a 625 Ms/s sampling rate.

To measure the gain and signal-to-noise ratio, the Thorlabs LED450LW LED was used as a low intensity visible light source. The LED was connected to an optical fibre, and the opposite end of the optical fibre was fed into the cylindrical enclosure shown in figure 5.7 to impinge photons onto the SiPM tile. The oscilloscope was then externally triggered in synchronization with the LED pulse, using a RS HMF2550 function generator. For measurements of the dark count rate without any external light, the oscilloscope was placed in self-trigger mode. Raw waveforms were saved from the oscilloscope for offline analysis.

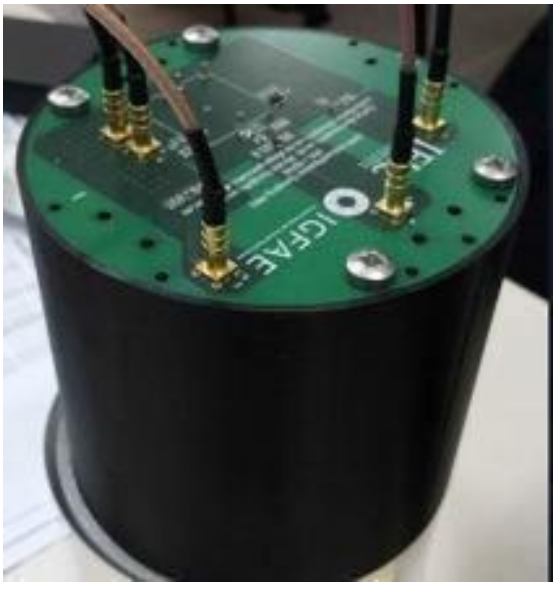

Figure 5.7: The SiPM tile and readout electronics were placed on a hollow plastic cylinder with the sensor facing inward, for electrical insulation, humidity protection and optical isolation.

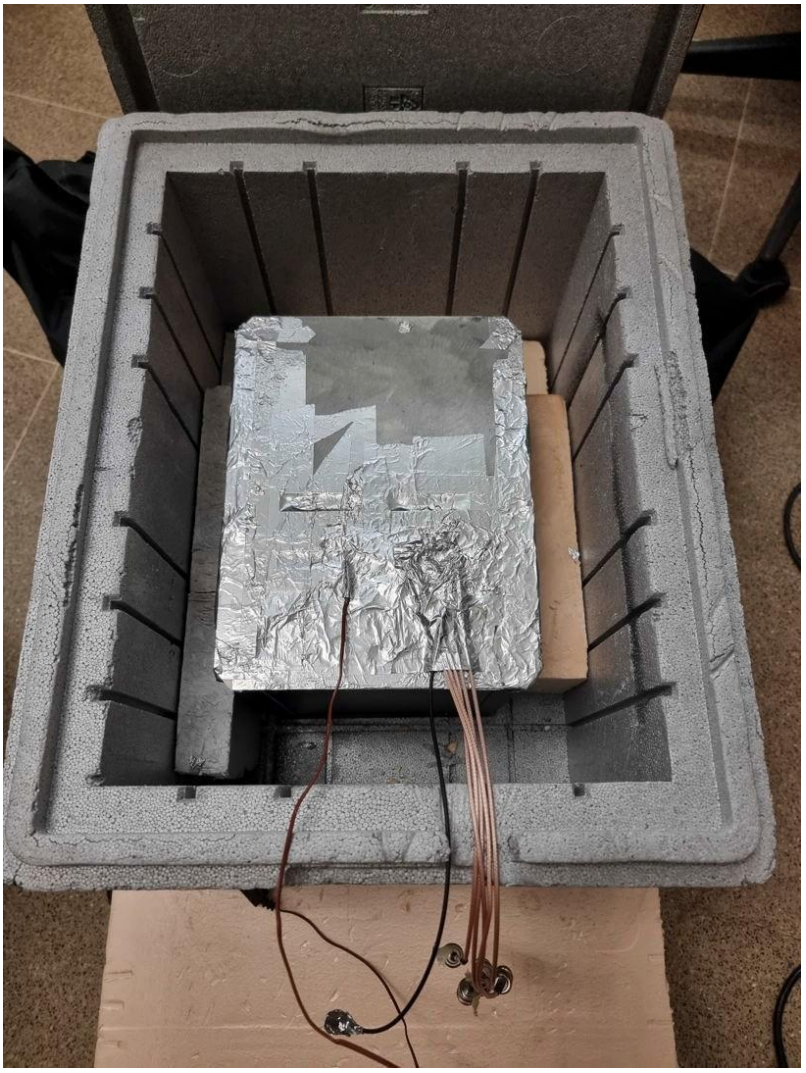

Figure 5.8: The thermally insulated polystyrene box, into which liquid nitrogen was filled to lower the temperature of the SiPM tile.

5.4 Measurements and results

5.4.1 Gain

The gain of the SiPM tile is the ratio of electric charge that is collected from the SiPM tile per photon interaction. The expected gain is in the range of 10^5 – 10^6, [14], and it was first necessary to determine if when the SiPM tile was coupled to the front-end electronics, it was operating to this expected level of performance in terms of relative gain and with a linear response.

The oscilloscope was set to acquire 3000 waveforms, each waveform with 1250 samples taken at an interval of 1.6 ns. It was triggered by the function generator which pulsed the LED that illuminated the SiPM tile. The waveforms were transferred to a computer, and analysed using the Python SciPy library [36]. An example of a waveform is shown in figure 5.9, and the superimposed traces from

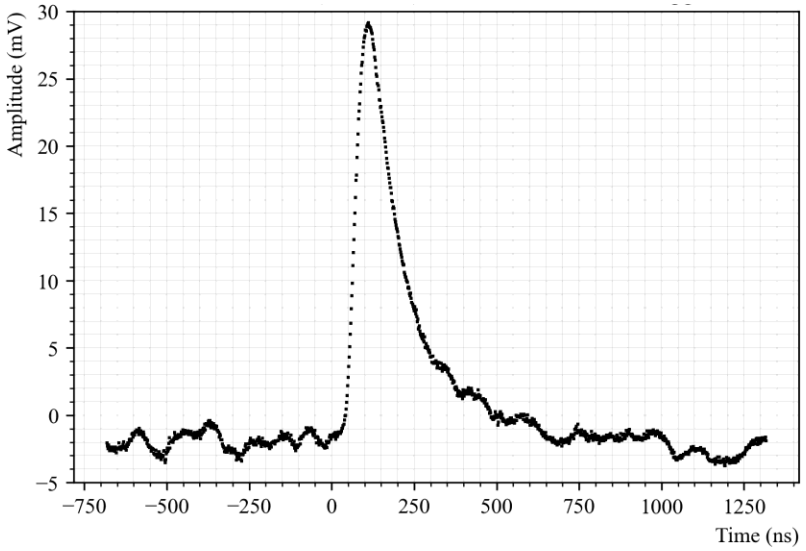

Figure 5.9: One waveform acquired from the oscilloscope, showing an output pulse from the readout electronics.

all 3000 waveforms is shown in figure 5.10.

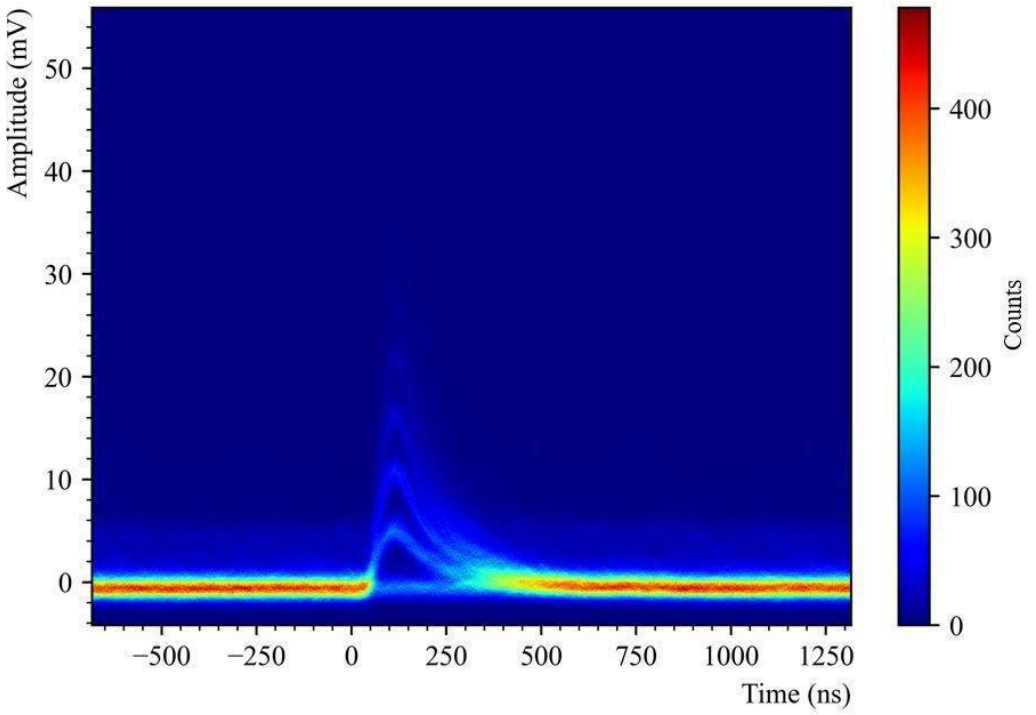

Figure 5.10: 3000 waveforms superimposed, from individual output pulses from the readout electronics. Distinct photon bands are visible, corresponding to the number of photons detected per event.

The amplitude of the post-trigger signals is proportional to the number of photons that were detected. Four discrete photon bands are clearly distinguishable. These are also displayed in the histogram shown in figure 5.11, where the frequency of each amplitude is plotted. The first peak at 0.33 mV corresponds to the pedestal, which gives a measure of the electronic noise when no photons are detected. A description of how the signal-to-noise ratio was obtained is described in section 5.4.2.

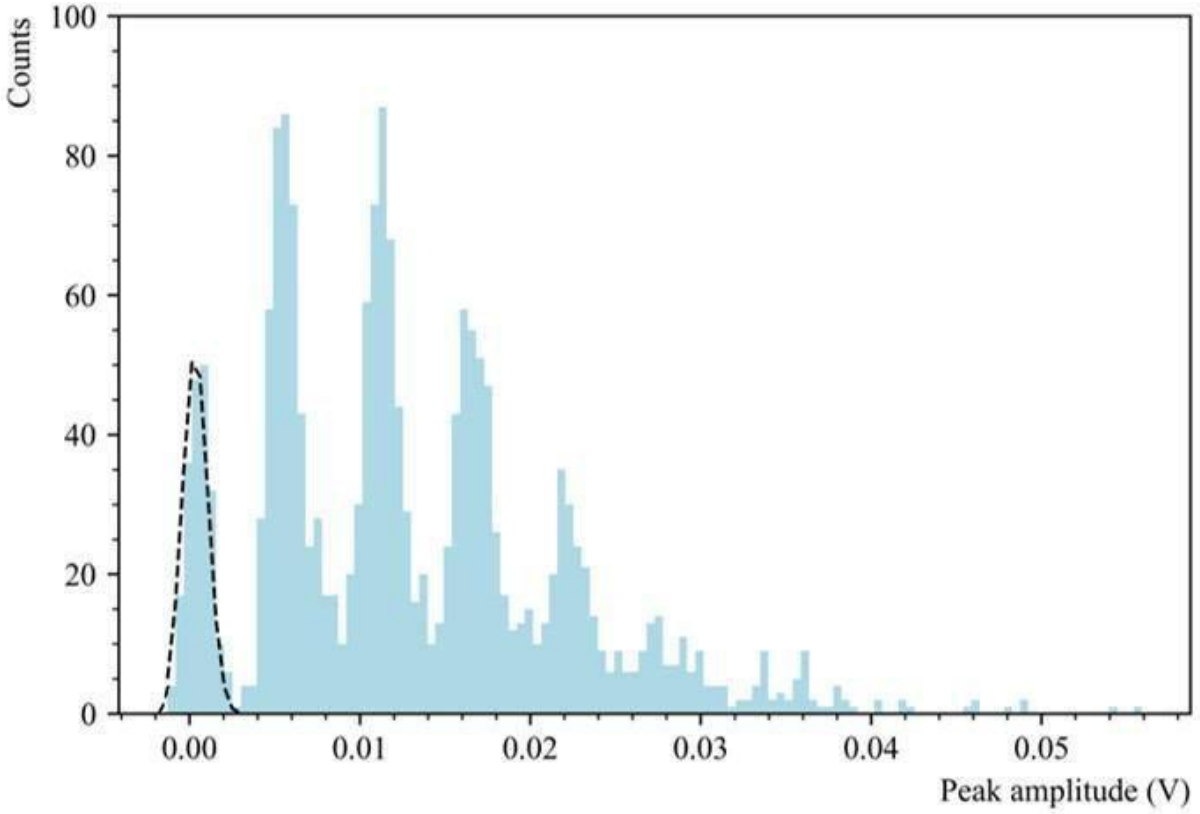

Figure 5.11: The counts distribution of the highest amplitudes from 3000 waveforms. The first peak is the pedestal, corresponding to no photon detections. The second peak is from single photon detection events, the third peak is from two photon detections, and so forth.

To determine the gain of the SiPM tile, the waveforms were integrated to find the total charge collected per trigger event. The charge integrals were then plotted on a frequency histogram, shown in figure 5.12. The first peak again corresponds to the pedestal, where no photons were detected. The second peak corresponds to the detection of one photon, the third peak corresponds to two photons, and the fourth peak to three photons. The mean values of each are plotted in figure 5.13, as a function of the photon number. The gain follows a Poisson distribution [37], therefore the uncertainty of each point was found by calculating the standard deviations.

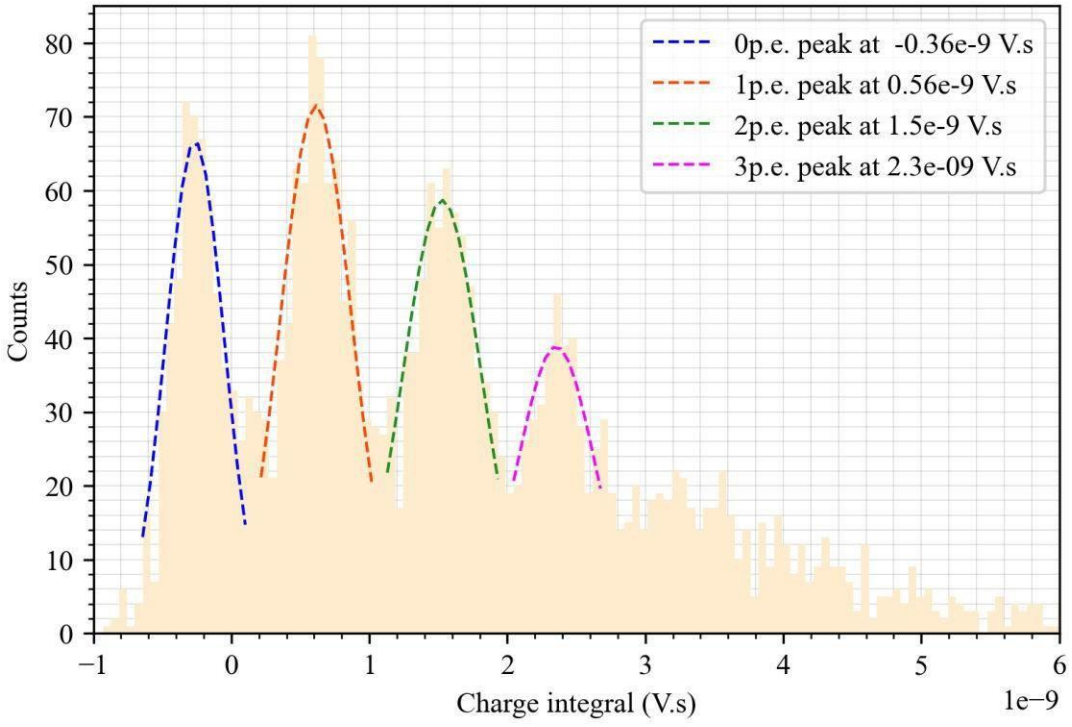

Figure 5.12: The charge integral distribution obtained from 3000 waveforms. The first peak is the pedestal, corresponding to no photon detections. The second peak is from single photon detection events, the third peak is from two photon detections, and the fourth peak is from three photon detections.

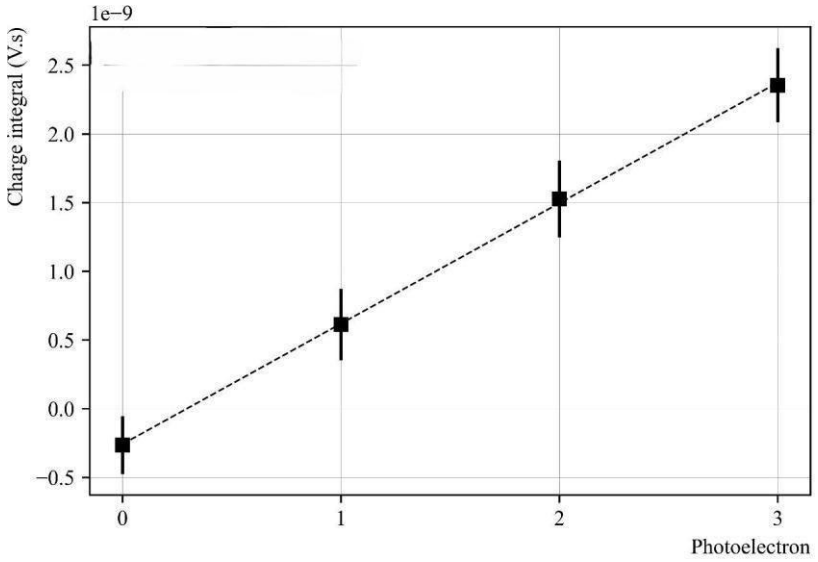

Figure 5.13: Charge integral as a function of number of photon detections.

The difference between the mean value of the single photon peak and the double photon peak, Qpp, can be used to give the total gain of the SiPM tile and amplification board, per photon interaction. The OPA847 Operational amplifier has a contribution towards the gain of 10^4 [34], and therefore the gain of the SiPM tile alone could be found using this relationship:

$$\text{SiPM gain} = \frac{Qpp}{q_0 \times \text{Amplifier gain}} \tag{5.1}$$

With this expression, where q_0 is the fundamental charge 1.6×10^{-19} C , the gain of the SiPM tile was calculated to be $(5.8750 \pm 0.0077)\times10^5$.

5.4.2 Signal-to-noise ratio and rise time

The baseline noise in the waveform is an intrinsic feature, caused by stochastic fluctuations. In the peak amplitude distribution histogram shown in figure 5.11, the pedestal (first peak) corresponds to no photon detections, and is a measure of the electronic noise. The following Gaussian function was fitted to the pedestal using the Python SciPy library [36], to obtain the standard deviation of the pedestal:

$$f(x) = a\, exp\,(-\frac{(x-b)^2}{2c^2}), \tag{5.2}$$

where a is the height of the peak, b is the location of the centre of the peak, and c is its' standard deviation which controls the width.

The signal-to-noise ratio is defined as the ratio of the distance between the peak amplitudes of the first photon peak ($A1p$) and the pedestal ($A0p$), and the standard deviation of the pedestal (σ_{0p}), using the following expression:

$$\text{Signal to noise ratio} = \frac{A_{1p} - A_{0p}}{\sigma_{0p}} \tag{5.3}$$

The pedestal peak was at 0.33 mV with a width of 0.75 mV. As the single photon peak was at 5.6 mV, this gave a signal-to-noise ratio of 7.03. The rise time of the signal was defined to be the time taken to go from 10% to 90% of the peak amplitude. This was analysed for each waveform. The distribution is shown in figure 5.14, with the mode rise time found to be at 45 ns.

5.4.3 Dark count rate

The dark count rate was measured by determining the rate of signals from the SiPM tile, when it had no external light incident upon it. The measurements were taken at a range of temperatures, from -35°C to -10°C. The oscilloscope was set to self-trigger mode to collect 3000 waveforms. As the SiPM tile was in darkness, each recorded event was due to a thermally generated dark count. The total acquisition time was saved by the oscilloscope.

Analysis of the waveforms was carried out offline, using a peak-finding algo-

rithm written in Python. The algorithm identified peaks based on a discrimination threshold of having an amplitude above half the single photon amplitude level (2.8 mV), as is the standardised procedure [15]. An example of the peak-discrimination output is shown in figure 5.15.

The SiPM tile consisted of 16 SiPMs, each with a sensitive area of 36 mm^2. The dark count rate in Hertz was calculated in terms of sensitive unit area, using the following expression:

$$\text{Dark count rate} = \frac{\text{Counts}}{\text{Acquistion time} \times (36\ mm^2 \times 16)} \tag{5.4}$$

The results as a function of temperature are shown in figure 5.16. At -35°C the dark count rate was 535±23 Hz/mm^2, and it increased with temperature to a level of 3237±57 Hz/mm^2 at -10°C.

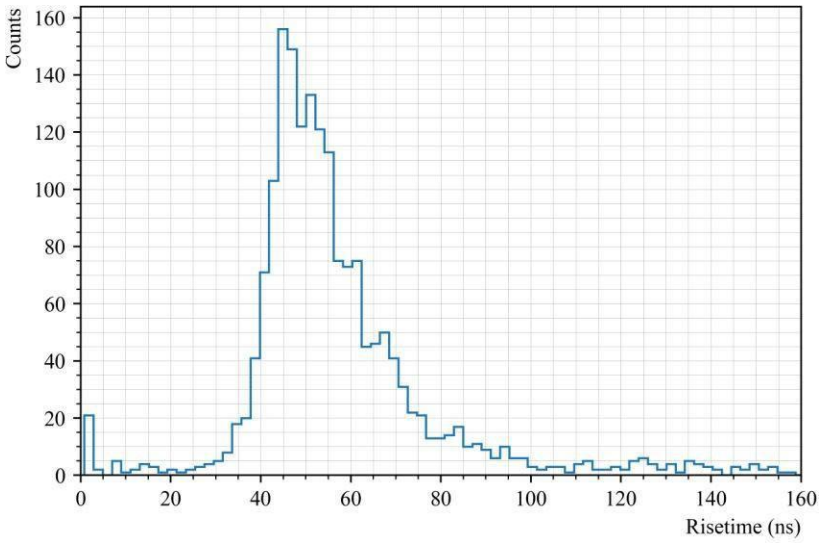

Figure 5.14: The distribution of rise times from 3000 signals, defined as the time for the signal to go from 10% to 90% of the peak amplitude.

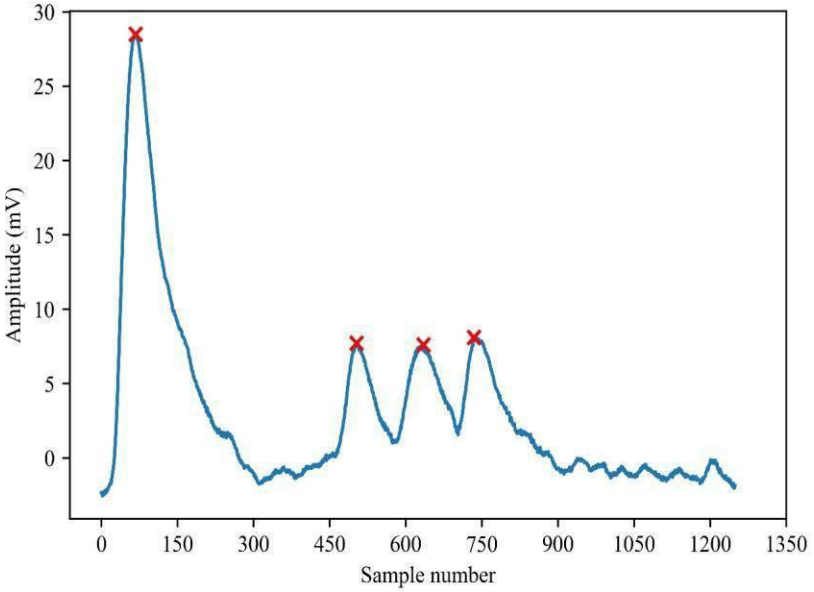

Figure 5.15: An example of the result from a peak-finding algorithm written in Python, to identify those which crossed the threshold of half the single photon amplitude. The red crosses mark the peaks which were identified.

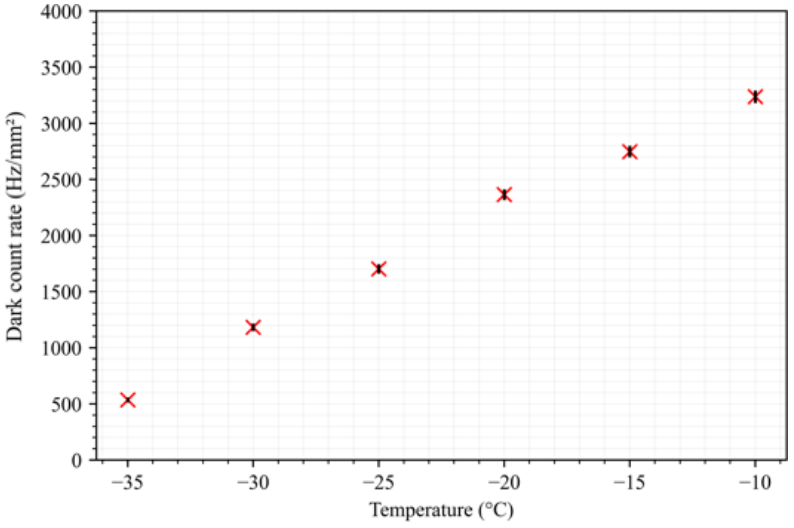

Figure 5.16: Dark count rate as a function of temperature. The plotted uncertainty values were found by obtaining the standard deviations.

Chapter 6

Geant4 simulations of light collection efficiency

6.1 Determining the number of detected photons

When an ionising particle interacts with molecules of the Ar:CF_4 gas mixture inside the optical time projection chamber to produce primary scintillation, only a fraction of the number of photons (N_p) that are produced will ultimately be detected by the SiPM. This can be approximated by the following expression:

$$N_p \simeq Y_{sc} \cdot \varepsilon_{SiPM} \cdot \eta \tag{6.1}$$

where Y_{sc} is the primary scintillation yield, ε_{SiPM} is the photon detection efficiency of the SiPM and η is their light collection efficiency.

The primary scintillation yield, Y_{sc}, is the average number of photons produced per unit of energy deposited by an ionising particle. As discussed in chapter 3, previous studies have reported that ~1400 photons are produced per MeV of an ionising particle interacting in a gas mixture of Ar:CF_4 (99:1). These photons are mostly produced in the range of 400-750 nm, peaking at 630 nm [5].

The photon detection efficiency of the SiPMs, ε_{SiPM}, can be found for a particular wavelength of light. For the S14161-6050HS-04 SiPM tile model that is under study and described in the previous chapter, the manufacture-stated photon detection efficiency for 630 nm is 25% [33].

It remains to determine the light collection efficiency, η. This parameter describes how many photons reach the photosensor, from the location where they were generated. It can be understood by simulating the propagation of photons through the detector in Geant4, under different conditions.

The light collection efficiency should be maximised, therefore the field cage of the GAT0 optical TPC was lined with a reflective layer of PTFE material. Photons are reflected off the PTFE surface, increasing the probability of them reaching the SiPMs. The light collection efficiency was simulated under different levels of PTFE reflectivity. Furthermore, in order to understand the level of coverage area required by SiPMs in the GAT0 optical TPC, various positions of where the photon is initially generated were simulated, to determine how distance effects the light collection efficiency.

6.2 PTFE reflectivity

PTFE material is a Lambertian (diffuse) reflector [38] – the reflected light distribution from its surface is the same, regardless of the viewing angle. It follows Lambert's Cosine Law, stating that the reflected light intensity is proportional to the cosine of the angle θ between the direction of observation and the surface normal. This is expressed as follows:

$$I = I_0 \cdot \cos(\theta), \tag{6.2}$$

where I is the intensity of reflected light in the direction of observation, I_0 is the intensity of reflected light in the direction normal to the surface, and θ is the angle between the two directions.

The measured reflectivity of PTFE at different photon wavelengths has been

reported in a study [39], where it was found to be 97-98% for light in the visible wavelength band, as seen in figure 6.1 where the uncertainties of the reflectance values are also plotted. Reflectance increases with longer wavelengths of light

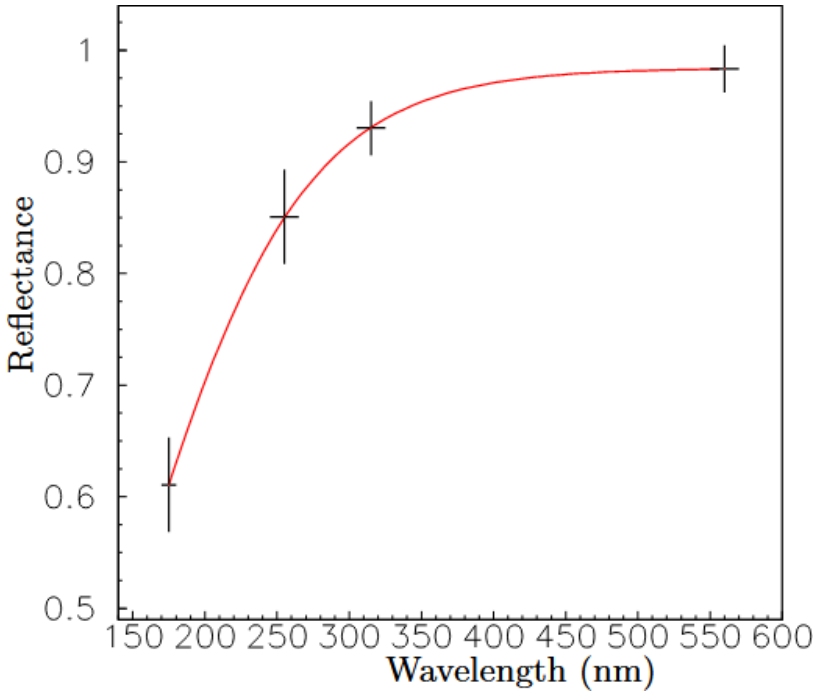

Figure 6.1: The measured reflectivity of a PTFE sample at a range of wavelengths [39].

due to more internal scattering, as longer wavelengths have a higher penetration depth into the PTFE.

However, variations as large as 2.7% have been reported within the same sample of PTFE [40]. Reflectivity can degrade from exposure to ambient light. Measurements of the reflectivity of the PTFE material within the GAT0 optical TPC have not been carried out, hence it was necessary to simulate a range of reflectance values, to determine the level of impact this has on the light collection efficiency.

6.3 Method of modelling the GAT0 optical TPC in Geant4

6.3.1 Geant4 overview

Geant4 [41] is an object-oriented toolkit written in the C++ programming language, used to simulate the passage of particles and radiation through matter with Monte Carlo methods. Within Geant4, a detector can be created with specified shapes and material properties, and the effects of physics interactions that can occur within the detector can be applied by adding relevant physics lists, to model the behaviour of defined particles. The detector geometry and particle tracks can be visualised in a graphical user interface.

6.3.2 Geometries and material properties

The basic geometry of the GAT0 optical TPC drift region where primary scintillation is generated and detected was made inside Geant4. In order to model a detector inside Geant4, volumes are created and placed inside a simulated world volume. For each volume, the material is specified, which then affects how the particle interacts with it according to the physical processes documented within Geant4. The GAT0 optical TPC was modelled by creating 3 volumes within the simulated world; the PTFE reflector, the SiPM tile and the gas mixture. An optical physics list was implemented, and the optical properties of each material were characterised, as described below.

The PTFE was modelled as a cylinder of length 139 mm, inner diameter 138.5 mm and thickness 10 mm. The centre of the cylinder was placed at the origin, as can be mapped on a cylindrical coordinate system. The optical properties of the PTFE were characterised by inputting its refractive index as 1.41 [42] and an initial reflectivity of 98%.

Two different geometries of SiPM coverages were modelled. The dimensions of the first were set so they covered the entire photosensor plane at the end of the PTFE cylinder; circular with a diameter of 138.5 mm and thickness 1.36 mm.

The dimensions of the second were according to that of the S14161-6050HS-04 model; a square with sides of length 25 mm, but the same thickness as the first of 1.36 mm. Aside from the shape and dimensions, both SiPM geometries had identical properties. The SiPMs were placed at one end of the PTFE cylindrical reflector, with its active surface at an axial distance of 69.8 mm from the centre of the reflector. The smaller square geometry was placed with its centre at polar coordinates $r = 12.5$ and $\theta = 90^{\circ}$, as illustrated in figure 6.2. When the SiPM tile

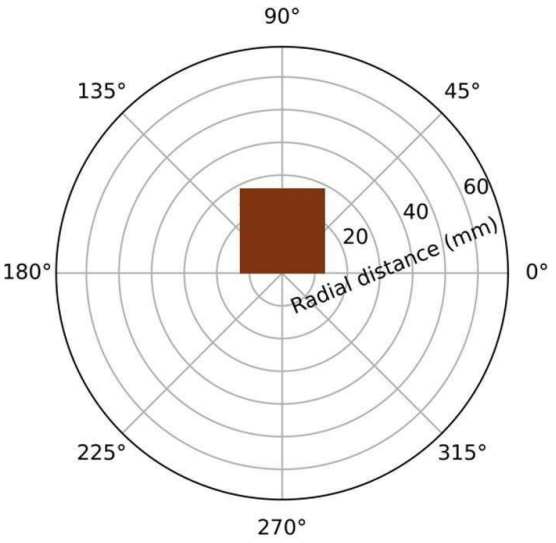

Figure 6.2: The polar coordinates of where the centre of the smaller SiPM tile geometry was placed in the Geant4 model was $r = 12.5$ and $\theta = 90^{\circ}$.

is installed in the GAT0 optical TPC, it would be located at an off-centred position due to it being mounted on the readout board, hence why these coordinates were set.

Both the PTFE reflector and the SiPMs were placed inside a volume of Ar:CF_4 gas, where light absorption was negligible and the refractive index was set to 1. The model was visualised in a graphical user interface in Geant4, as can be seen in figure 6.3.

6.3.3 Event generation

By generating an event, photons can be propagated through the detector with preset initial conditions. For each event, 20,000 photons of 630 nm were created, with a randomised direction. The photons were generated at different positions along the radial, azimuthal and height (r, θ, z) cylindrical coordinates of the model. The reflectivity of the PTFE was varied, including a simulation with 0% reflectance. Tracks could be visualised in the graphical user interface, as seen in figure 6.4.At the end of each event, an output file was retrieved, which had recorded the coordinates of where the photons which had reached the SiPMs had been detected.

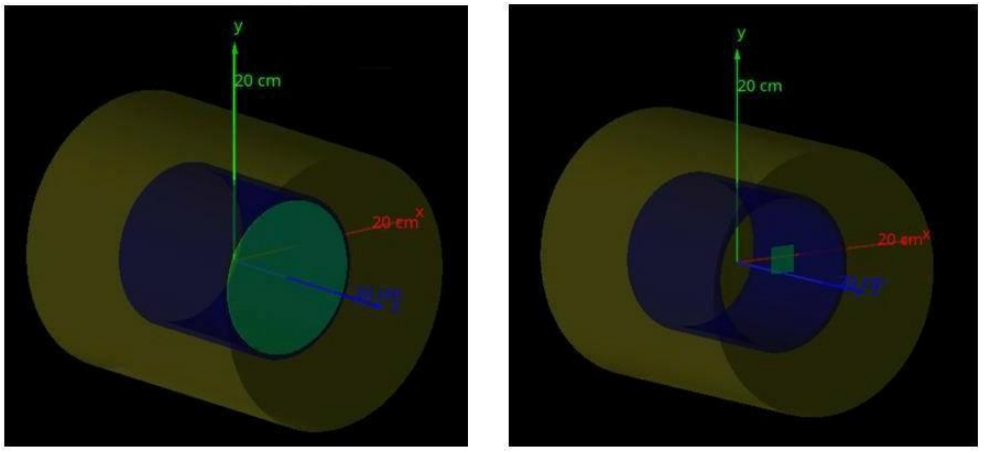

Figure 6.3: The two different SiPM coverage geometries that were simulated, visualised in the Geant4 graphical user interface.

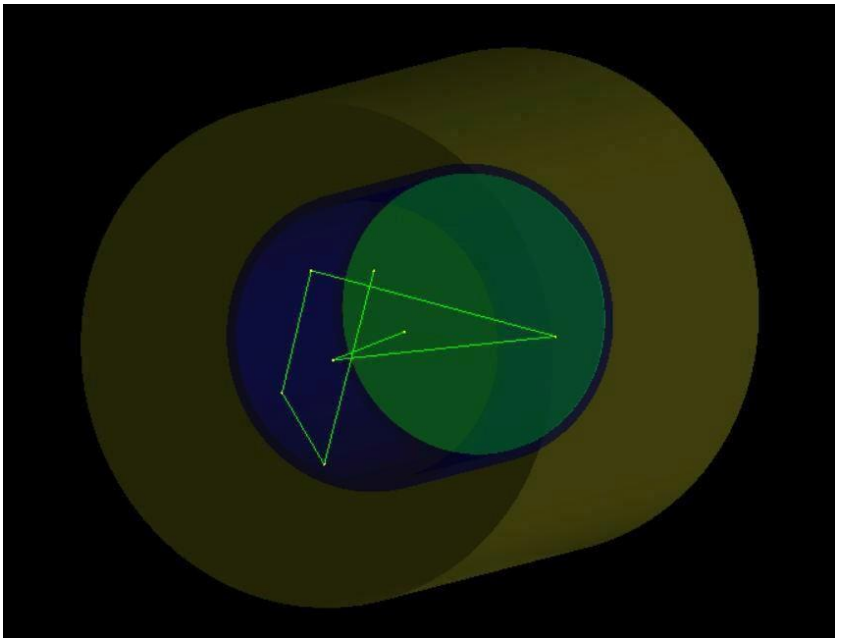

Figure 6.4: The trajectory of a simulated photon.

6.4 Results

6.4.1 Analytical verification

The intensity of light detected by the SiPMs is a function of the solid angle subtended by the SiPMs at the position of photon generation. To verify the Geant4 simulation model, analytical calculations of the light collection efficiency were carried out using the formula for a solid angle subtended by a circle [43]:

$$\Omega = 2\pi \cdot \left(1 - \frac{z}{\sqrt{R^2_{\text{circle}} + z^2}}\right) \tag{6.3}$$

where the radius, R, of 69.3 mm was used according to that of the large SiPMs geometry that covered the entire photosensor plane and z was the axial distance

to it.

A range of axial distances were calculated, from 9.8 mm to 129.8 mm between the point where the photons were generated and the surface of the SiPMs, and the corresponding simulations were ran with a reflectivity of 0%. The analytical efficiency, $\varepsilon_{\text{analyt}}$ was calculated using the subtended solid angle:

$$\varepsilon_{\text{analyt}} = \frac{\Omega}{4\pi} \times 100\% \tag{6.4}$$

This was compared to the light collection efficiency, η, computed from the simu lation:

$$\eta = \frac{\text{Number of Geant4 detections}}{\text{Number of generated photons}} \times 100\% \quad (6.5)$$

The standard deviations of the simulated light collection efficiencies were $\sigma \leq 0.3\%$. The efficiencies follow a Binomial distribution, as is outlined in [44]:

$$\sigma = \sqrt{\text{Number of Geant4 detections} \times (1 - \eta)} \quad (6.6)$$

The results of the simulations, as seen in figure 6.5, were in good agreement with the analytical efficiencies, thus verifying the model.

Thereafter, the reflectivity of the PTFE was updated to 98%, whereby an increase (from 14.5 ±0.1% to 47.8 ±0.4%) of 33.3 ±0.4% was seen in the efficiency, when photons were originating from the centre of the cylinder. This difference was reduced to 28.7±0.4% at the smallest distance between the SiPM and photon generation point of 9.8 mm , where the photons had a higher probability of reaching the SiPMs without any reflective surface. When photons were generated at the furthest axial distance (129.8 mm), the difference in efficiency with and without a reflective layer was at the lowest point of 19.3±0.3%, as a higher proportion of light was escaping the far end of the cylinder without being detected. A visualization of the changing photon hit distributions can be seen in figure 6.6 and the results are plotted in figure 6.5.

6.4.2 Reflectivity

The reflectivity of the PTFE was varied from 90% to 99% and the corresponding light collection efficiency was simulated, with photons generated from the centre of the cylinder. The efficiency increased from 41.5±0.3% (90% PTFE reflectivity) to 48.6±0.4% (99% PTFE reflectivity), with a linear increase as shown in figure 6.7.

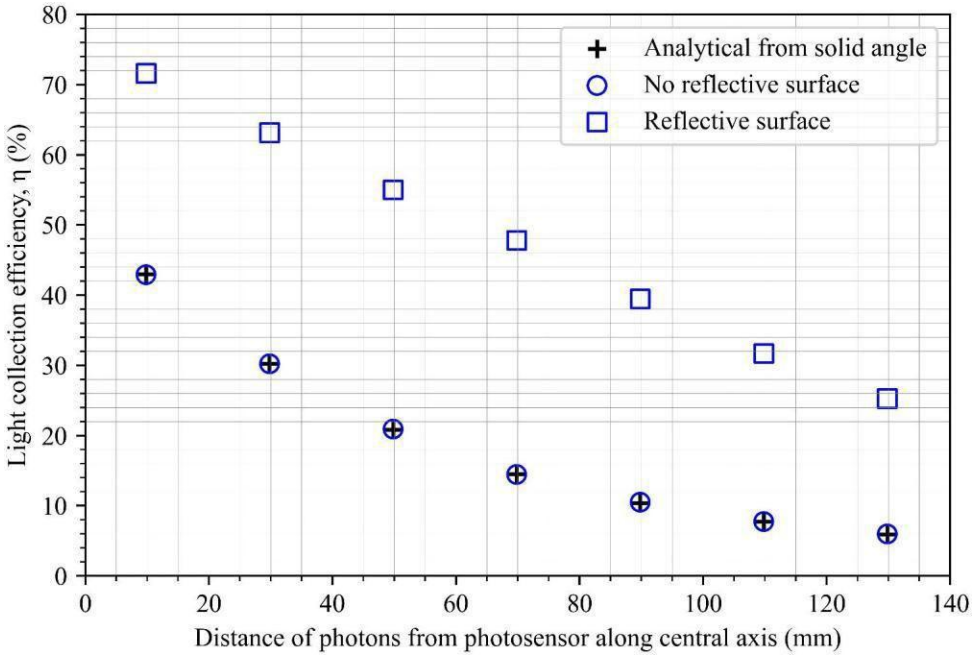

Figure 6.5: Light collection efficiency as a function of distance along the central axis of the PTFE cylinder, with 0% and 98% PTFE reflectivity. Analytical efficiencies calculated from the subtended solid angle are also shown. Error bars calculated from equation 6.6, assuming a binomial distribution, are smaller than the data markers with values of $\sigma \leq 0.3\%$.

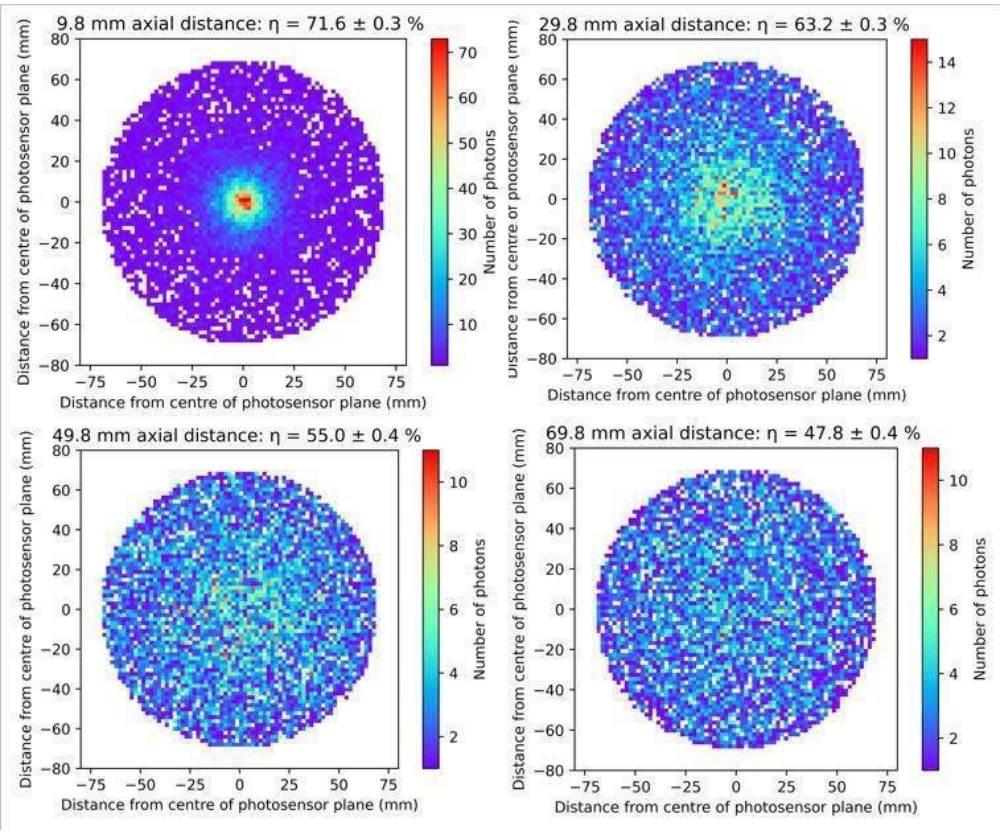

Figure 6.6: A visualization of the changing photon hit distributions, from the photons being generated at an increasing axial distance from the large SiPMs geometry.

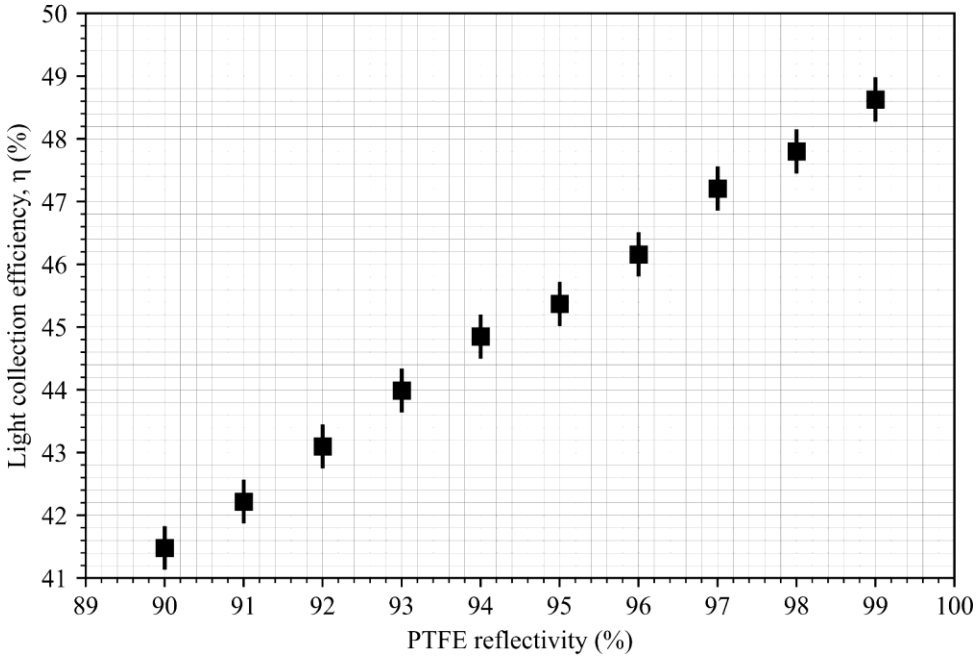

Figure 6.7: The light collection efficiency as a function of PTFE reflectivity, ranging from 90% - 99%. Error bars were calculated assuming a binomial distribution, using equation 6.6.

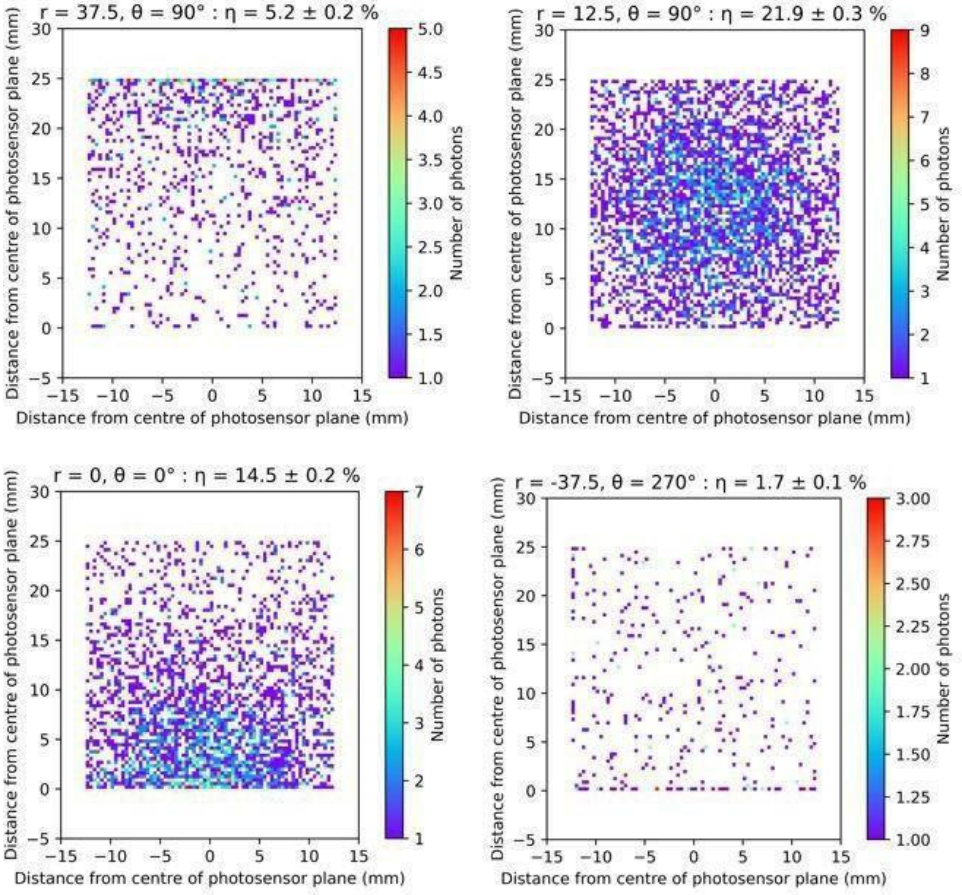

Figure 6.8: A visualization of the changing photon hit distributions on the surface of the smaller SiPMs geometry, from the photons being generated at different radial distances

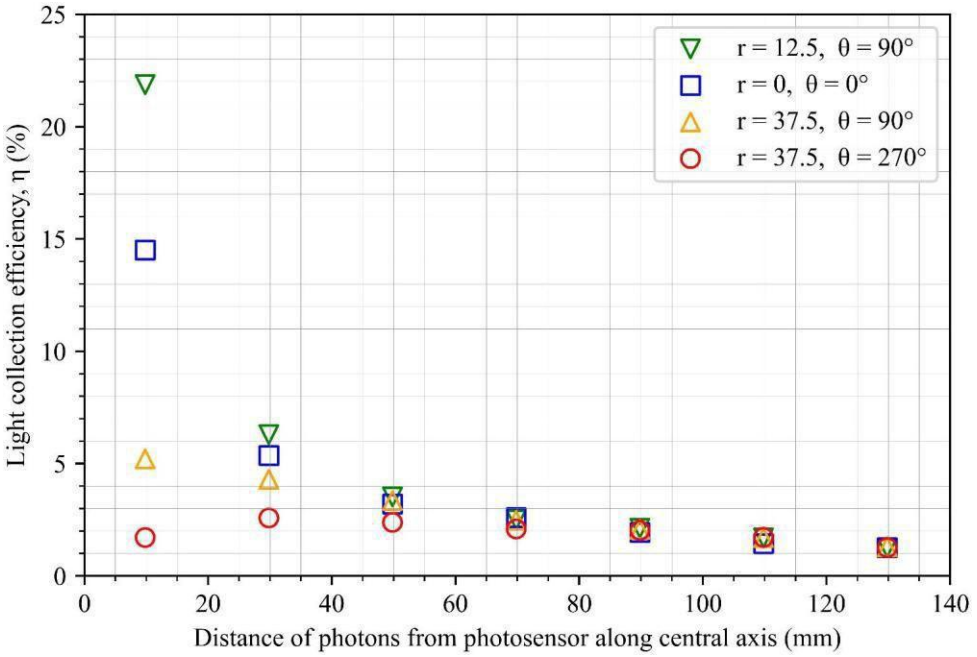

Figure 6.9: The light collection efficiency resulting from photons being generated at increasing axial distances from the SiPMs. 4 different radial positions were simulated for each axial distance. Uncertainties calculated assuming a binomial distribution using equation 6.6 are not visible on the scale, with values of $\sigma \leq 0.3\%$

6.4.3 Initial position of photon

The Geant4 was updated with the dimensions of the Hamamatsu S14161-6050HS-04 model, of a surface area of 25 mm^2 , positioned as illustrated in figure 6.2 . The simulation was ran with a reflectivity of 98%, to understand the effect the position where the photon was generated had on the light collection efficiency, with a reduced active detection surface area. Photons were generated at positions in increments of 20 mm along the central axis of the model, from 9.8 mm between the SiPMs and photon generation point up to 129.8 mm. For each axial position, the radial distances and azimuth angles were varied, including 12.5 mm ($\theta = 90^\circ$), 37.5 mm ($\theta = 90^\circ$), 37.5 mm ($\theta = 270^\circ$) and the central position. A visualisation of how the photon hit distribution changed can be seen in figure 6.8, and the results in figure 6.9.

When photons were generated normal to the centre of the SiPMs at the closest axial distance of 9.8 mm, the efficiency peaked with a value of 21.9±0.3%. At the furthest axial distance of 129.8 mm, this reduced to 12.5 ±0.1%. Here, the efficiency converged to be between 12.5 ±0.1% to 13.0 ±0.1% , regardless of the radial coordinate, as the light escaping from the cylinder was the predominant effect. This effect can also be seen when photons were generated at the closest axial distance (9.8 mm) but the furthest radial position (37.5 mm, $\theta = 270^\circ$) from the SiPMs – there was a drop in efficiency of 0.9±0.1% compared to when they were generated further away at 29.8 mm from the same radial point.

Chapter 7

Conclusions

The GAT0 optical TPC was used to demonstrate imaging of alpha particle ionisation tracks in an Ar:CF_4 gaseous mixture at 1 bar, using a double thick GEM stack in GAT0 for the first time. Future work will increase the pressure to 5 bar, to see if there is adequate secondary scintillation light at high pressures for optical imaging, as is a requirement for the ND-GAr detector.

Photosensors in ND-GAr will be used to determine the absolute timing of neutrino interactions from the primary scintillation signals, therefore the time resolution of the photosensor limits how precisely this information can be retrieved. SiPMs can operate at high pressures and in a magnetic field as is required for ND-GAr, but they have small sensitive areas and a large-area coverage is needed. If several SiPMs are installed, then it would be necessary to combine readout channels, as they cannot be readout individually due to power and space constraints. Typically, combining readout channels lowers the time resolution due to a higher capacitance in the front-end electronics. This is seen in one way via a degradation in the signal-to-noise ratio. A readout electronics board that ganged (combined) 16 readout channels was experimentally tested with the chosen Hamamatsu 25 mm^2 S14161-6050HS-04 model SiPM tile, and the gain was found to be performing within the manufacture specifications of 10^5 - 10^6. The signal-to-noise ratio was 7, which is high enough to not limit the time resolution. The dark count

rate also reduces the time resolution, and so this was measured as a function of temperature, and found to be ∼500 at -35 ˚C. Active cooling schemes to reduce the dark count rate to tolerable levels are being investigated.

A PTFE reflector around the GAT0 TPC field cage was simulated in Geant4, to assess the primary scintillation light collection efficiency of the Hamamatsu 25 mm^2 S14161-6050HS-04 model SiPM tile, when it is installed within the GAT0 optical TPC. Assuming 98% PTFE reflectivity and a scintillation yield of ∼1400 photons/MeV in Ar:CF_4 gas [5], up to ∼ 77 photon detections per MeV of deposited energy can be expected. This was calculated using equation 6.1 and the efficiency output from the simulated model that has been presented with photons generated 9.8 mm away from the SiPMs. If the SiPMs area coverage could be extended to cover the entire photosensor plane by installing multiple SiPM tiles at the end of the PTFE cylinder, this number would increase to ∼250 photon detections per MeV of deposited energy.

Bibliography

1. *Deep Underground Neutrino Experiment* en-US. https://www.dunescience.org/ (2025).
2. Abud, A. A. *et al.* Deep Underground Neutrino Experiment (DUNE) Near Detector Conceptual Design Report. en. *Instruments* 5. Number: 4 Publisher: Multidisciplinary Digital Publishing Institute, 31. issn: 2410-390X. https://www.mdpi.com/2410-390X/5/4/31 (2025) (Dec. 2021).
3. Saá-Hern´andez, A. *et al. On the determination of the interaction time of GeV neutrinos in large argon gas TPCs* en. arXiv:2401.09920 [physics]. Nov. 2024. http://arxiv.org/abs/2401.09920 (2025).
4. Chandrasekharan, R., Knecht, A., Messina, M., Regenfus, C. & Rubbia, A. *High efficiency detection of argon scintillation light of 128 nm using LAAPDs* in *IEEE Nuclear Science Symposium Conference Record, 2005* 1. ISSN: 1082-3654 (Oct. 2005), 181–185. https:// ieeexplore. ieee. org/ document/ 1596232 (2025).
5. Amedo, P., Leardini, S., Saá-Hern´andez, A. & González-D´ıaz, D. *Primary scintillation yields induced by $$ particles in gasmixtures of Argon/CF$3em at 9.5 bar* arXiv:2410.17853 [physics]. Oct. 2024. http://arxiv.org/abs/2410.17853 (2025).
6. Nygren, D. R. The Time Projection Chamber: A New 4 pi Detector for Charged Particles. *eConf* C740805 (eds Kadyk, J., Nygren, D., Wenzel, W. & Winkelmann, F.) 58 (1974).
7. *Working Principle of a TPC* https://www.lctpc.org/e8/e57671 (2025).

8. Leo, W. R. *Techniques for Nuclear and Particle Physics Experiments: A How-to Approach* en. isbn: 978-3-540-57280-0 978-3-642-57920-2. https://link.springer.com/10.1007/978-3-642-57920-2 (2025) (Springer, Berlin, Heidelberg, 1994).

9. Scharenberg, L. S. Next-Generation Electronics for the Read-Out of Micro-Pattern Gaseous Detectors. de.

10. D´ıaz, D. G., Simón, J. M.-A. & D´ıaz, D. G. SCINTILLATING NEW PHYSICS WITH THE PRESSURIZED NDGAR TPC AT THE DUNE NEAR DETECTOR COMPLEX. en.

11. Sauli, F. GEM: A new concept for electron amplification in gas detectors. *Nuclear Instruments and Methods in Physics Research Section A: Accelerators, Spectrometers, Detectors and Associated Equipment* 386, 531–534. issn: 0168-9002. https://www.sciencedirect.com/science/article/pii/S0168900296011722 (2025) (Feb. 1997).

12. Sauli, F. The gas electron multiplier (GEM): Operating principles and applications. *Nuclear Instruments and Methods in Physics Research Section A: Accelerators, Spectrometers, Detectors and Associated Equipment. Special Issue in memory of Glenn F. Knoll* 805, 2–24. issn: 0168-9002. https://www.sciencedirect.com/science/article/pii/S0168900215008980 (2025) (Jan. 2016).

13. Raether, H. *Electron avalanches and breakdown in gases* eng. Open Library ID: OL26550760M (Butterworth, London, 1964).

14. *Physics and operation of the MPPC silicon photomultiplier — Hamamatsu Photonics* en. https://hub.hamamatsu.com/us/en/technical-notes/mppc-sipms/physics-and-operation-of-the-MPPC-silicon-photomultiplier.html (2025).

15. Otte, A. N., Garcia, D., Nguyen, T. & Purushotham, D. Characterization of three high efficiency and blue sensitive silicon photomultipliers. *Nuclear Instruments and Methods in Physics Research Section A: Accelerators, Spectrometers, Detectors and Associated Equipment* 846, 106–125. issn: 0168-

9002. https://www.sciencedirect.com/science/article/pii/S0168900216309901 (2025) (Feb. 2017).

16. (PDF) Muon Counting using Silicon Photomultipliers in the AMIGA detector of the Pierre Auger Observatory. en. *ResearchGate*. issn: 1748-0221. https://www.researchgate.net/publication/314218790_Muon_Counting_using_Silicon_Photomultipliers_in_the_AMIGA_detector_of_the_Pierre_Auger_Observatory (2025) (May 2025).

17. Spieler, H. *Semiconductor Detector Systems* isbn: 978-0-19-852784-8 (Oxford University Press, Oxford, 2005).

18. *Silicon photomultipliers (SiPM): The ultimate photosensor? — Hamamatsu Photonics* en. https:// hub. hamamatsu. com/ us/ en/ technical- notes/ mppc- sipms/silicon- photomultipliers- the- ultimate- photosensor. html (2025).

19. Sigmund, P. *Particle Penetration and Radiation Effects* (eds Cardona, M. *et al.*) isbn: 978-3-540-31713-5 978-3-540-31718-0. http://link.springer.com/10.1007/3-540-31718-X (2025) (Springer, Berlin, Heidelberg, 2006).

20. Tawara, H., Ishida, N., Kikuchi, J. & Doke, T. Measurements of the *W* values in argon, nitrogen, and methane for 0.93 to 5.3 MeV alpha particles. *Nuclear Instruments and Methods in Physics Research Section B: Beam Interactions with Materials and Atoms* 29, 447–455. issn: 0168-583X. https://www.sciencedirect.com/science/article/pii/0168583X87900553 (2025) (Dec. 1987).

21. Rolandi, L., Riegler, W. & Blum, W. *Particle Detection with Drift Chambers* en. isbn: 978-3-540-76683-4 978-3-540-76684-1. https://link.springer.com/10.1007/978-3-540-76684-1 (2025) (Springer, Berlin, Heidelberg, 2008).

22. Ertley, C. *STUDYING THE POLARIZATION OF HARD X-RAY SOLAR FLARES WITH THE GAMMA RAY POLARIMETER EXPERIMENT (GRAPE)* in. 223. ADS Bibcode: 2014AAS...22311803E (Jan. 2014), 118.03. https://ui.adsabs.harvard.edu/abs/2014AAS...22311803E (2025).

23. Sabbatucci, L. & Salvat, F. Theory and calculation of the atomic photoeffect. *Radiation Physics and Chemistry* 121, 122–140. issn: 0969-806X. https: // www. sciencedirect. com/ science/ article/ pii/ S0969806X15300815 (2025) (Apr. 2016).

24. Kolanoski, H. & Wermes, N. *Particle Detectors* isbn: 978-0-19-885836-2 (Oxford University Press, June 2020).

25. Amedo, P. *et al.* Observation of strong wavelength-shifting in the argon-tetrafluoromethane system. English. *Frontiers in Detector Science and Technology* 1. Publisher: Frontiers. issn: 2813-8031. https://www.frontiersin.org/journals/detector-science-and-technology/articles/10.3389/fdest.2023.1282854/full (2025) (Dec. 2023).

26. Dhanumalayan, E. & Joshi, G. M. Performance properties and applications of polytetrafluoroethylene (PTFE)—a review. en. *Advanced Composites and Hybrid Materials* 1, 247–268. issn: 2522-0136. https://doi.org/10.1007/s42114-018-0023-8 (2025) (June 2018).

27. *Retiga R6 — Teledyne Vision Solutions* en-US. https://www.teledynevisionsolutions.com/products/retiga-ccd-family?vertical=tvs-photometrics&segment=tvs (2025).

28. Kondev, F., Wang, M., Huang, W., Naimi, S. & Audi, G. The NUBASE2020 evaluation of nuclear physics properties *. en. *Chinese Physics C* 45. Publisher: Chinese Physical Society and the Institute of High Energy Physics of the Chinese Academy of Sciences and the Institute of Modern Physics of the Chinese Academy of Sciences and IOP Publishing Ltd, 030001. issn: 1674-1137. https:// dx. doi. org/ 10 . 1088 / 1674 - 1137 / abddae (2025) (Mar. 2021).

29. Malain, D. & Kanchana, P. Evaluation of radiation safety for ionization chamber smoke detectors containing Am-241. en. *Journal of Physics: Conference Series* 1285. Publisher: IOP Publishing, 012047. issn: 1742-6596. https: //dx.doi.org/10.1088/1742-6596/1285/1/012047 (2025) (Aug. 2019).

30. Zhi, W. *et al. Front-end electronics development of large-area SiPM arrays for high-precision single-photon time measurement* arXiv:2403.02948 [physics] version: 1. Mar. 2024. http://arxiv.org/abs/2403.02948 (2025).

31. Acerbi, F. *et al.* Characterization of Single-Photon Time Resolution: From Single SPAD to Silicon Photomultiplier. *IEEE Transactions on Nuclear Science* 61, 2678–2686. issn: 1558-1578. https : / / ieeexplore . ieee . org / document/6882845 (2025) (Oct. 2014).

32. Marano, D. *et al.* Silicon Photomultipliers Electrical Model Extensive Analytical Analysis. *IEEE Transactions on Nuclear Science* 61, 23–34. issn: 1558-1578. https:// ieeexplore. ieee. org / document / 6661445 (2025) (Feb. 2014).

33. Hamamatsu. *MPPC (Multi-Pixel Photon Counter) S14160/S14161 series* (). https://www.hamamatsu.com/eu/en/product/optical- sensors/mppc/mppc_mppc-array/S14161-6050HS-04.html (2025).

34. *OPA847 — Buy TI Parts — TI.com* https :/ / www . ti . com / product / OPA847/part-details/OPA847IDR (2025).

35. *THS4131 data sheet, product information and support — TI.com* https: //www.ti.com/product/THS4131 (2025).

36. Virtanen, P. *et al.* SciPy 1.0: fundamental algorithms for scientific computing in Python. en. *Nature Methods* 17. Publisher: Nature Publishing Group, 261–272. issn: 1548-7105. https://www.nature.com/articles/s41592- 019-0686-2 (2025) (Mar. 2020).

37. Klanner, R. Characterisation of SiPMs. en. *Nuclear Instruments and Methods in Physics Research Section A: Accelerators, Spectrometers, Detectors and Associated Equipment* 926, 36–56. issn: 01689002. https://linkinghub. elsevier.com/retrieve/pii/S0168900218317091 (2025) (May 2019).

38. Pedrotti, F. L. & Pedrotti, L. S. *Introduction to Optics* en. Google-Books-ID: UXyPQgAACAAJ. isbn: 978-0-13-016973-0 (Prentice Hall, 1993).

39. Silva, C. *et al.* Reflectance of Polytetrafluoroethylene (PTFE) for Xenon Scintillation Light. *Journal of Applied Physics* 107. arXiv:0910.1056 [physics], 064902. issn: 0021-8979, 1089-7550. http:// arxiv. org/ abs/ 0910 . 1056 (2025) (Mar. 2010).

40. Ghosh, S. *et al.* Dependence of polytetrafluoroethylene reflectance on thickness at visible and ultraviolet wavelengths in air. *Journal of Instrumentation* 15. arXiv:2007.06626 [physics], P11031–P11031. issn: 1748-0221. http://arxiv.org/abs/2007.06626 (2025) (Nov. 2020).

41. Agostinelli, S. *et al.* Geant4—a simulation toolkit. *Nuclear Instruments and Methods in Physics Research Section A: Accelerators, Spectrometers, Detectors and Associated Equipment* 506, 250–303. issn: 0168-9002. https:// www. sciencedirect. com/ science/ article/ pii/ S0168900203013688 (2025) (July 2003).

42. Bichon, J. *et al. Complex refractive index determination of PTFE, TPX and polypropylene windows for TeraHertz broadband spectroscopy* in *2022 47th International Conference on Infrared, Millimeter and Terahertz Waves (IRMMW-THz)* ISSN: 2162-2035 (Aug. 2022), 1–2. https://ieeexplore.ieee.org/abstract/document/9895520 (2025).

43. Baghani, H. R. & Aminafshar, B. An inter-comparison between calculated solid angle for different geometrical correlations of source-detector through analytical and Monte Carlo approaches. en. *Indian Journal of Physics.* issn: 0974-9845. https://doi.org/10.1007/s12648-024-03453-4 (2025) (Oct. 2024).

44. Cowan, G. & Physics, R. Error analysis for efficiency.